

Statistics of Multi-Instrument Observations of Solar Flares

James Kavanagh-Cranston

A report presented for
MSci Physics with Astrophysics

Astrophysics Research Centre
School of Mathematics and Physics
Queen's University Belfast

Abstract

Multi-wavelength observations offer an advanced insight into the mechanics involved in solar flares. This study uses the observation metadata of eight instruments and a combination of the *Geostationary Observational Environmental Satellite (GOES)* and *Heliophysics Events Knowledgebase (HEK)* flare lists to search for simultaneous space-based observations of flares, cataloguing a total of 14,458 C1.0< events between 2010-April-30 and 2019-May-30. It was found that 72 flares were simultaneously observed by seven or more instruments and 98.5% of flares were observed by at least one instrument. On average, each flare was observed by three instruments simultaneously, demonstrating the significant efforts to produce multi-wavelength observations through coordination efforts such as the *Max Millennium Program of Solar Flare Research*. All of the instruments included in this study met or exceeded their expected values for success rate calculated using instrument field-of-view and duty cycle estimates. A total of four flares were found to have been observed by all eight instruments including a newly discovered C2.6 flare on 2013-Nov-09. This flare presents significant research potential with very good coverage in both wavelength and time.

Contents

Abstract	i
List of Figures	vi
List of Tables	vii
Acronyms	viii
1 Introduction	1
1.1 Background	2
1.1.1 The Photosphere	3
1.1.2 The Chromosphere	3
1.1.3 The Corona	4
1.1.4 Sunspots & Active Regions	4
1.1.5 The Standard Model of a Solar Flare	4
1.2 The Importance of Multi-Wavelength observations	5
1.3 Challenges of Multi-Wavelength Observations	7
1.4 Outstanding Questions in Solar Flare Physics	9
2 Method	10
2.1 Initial Parameters	10
2.2 Combining Flare Lists	12
2.2.1 Selecting Existing Flare Lists	12
2.2.2 Joining Existing Flare Lists	13
2.3 Determining an Instrument's Observation of a Solar Flare	13
2.3.1 Reuven Ramaty High Energy Solar Spectroscopic Imager	13
2.3.2 Fermi Gamma-Ray Burst Monitor	14
2.3.3 Solar Dynamics Observatory - Extreme Ultraviolet Variability Experiment	16
2.3.4 Hinode - EUV Imaging Spectrometer	17
2.3.5 Hinode - Solar Optical Telescope	17
2.3.6 Hinode - X-Ray Telescope	18
2.3.7 Interface Region Imaging Spectrograph	18
3 Results	18
3.1 Statistics of Multi-Wavelength Observations	18
3.1.1 Expected Instrument Success Rates	22
3.1.2 Newly Discovered Exceedingly Well-Observed Flare	24

4	Summary	28
4.1	Further Study	28
4.2	Conclusions	29
A	Mount-Wilson Classification of Active Regions	i
B	Two Pointer Approach for Finding Interval Intersections	ii
C	RHESSI Flare Flag Inaccuracies	iv
References		v

List of Figures

1	A plot describing the temperature and density of the outer layers of the Sun; the photosphere, chromosphere, transition region and the corona. T_e represents the plasma temperature, N_e is the electron density and N_H is the density of neutral Hydrogen. (Aschwanden, 2005)	3
2	<i>Left:</i> Diagram depicting the outer layers of the Sun with layer thicknesses from Williams (2022). <i>Right:</i> Cartoon of the standard model of a solar flare. The magnetic loop can be seen extending into the corona, meeting the chromosphere at the footpoints depicted as checkered areas at the ends of the loops. (Shibata, 2015)	5
3	Time evolution of the flare SOL2001-10-19T01:05 (X1.6) in multiple X-ray, EUV, and radio wavelengths. From shortest to longest wavelength: the <i>blue</i> line represents the hard X-ray emission as measured by the 100 keV band of the <i>Yohkoh Wide Band Spectrometer</i> (WBS); the <i>green</i> line represents emission measured by the <i>Yohkoh Hard X-ray Telescope</i> (HXT) in its 15-24 keV band; the <i>red</i> line represents the soft X-ray emission measured by the 1-8 Å channel of the <i>GOES X-Ray Sensor</i> (XRS); and the <i>black</i> line represents the shortest-wavelength radio emissions (6.6 GHz) measured by the <i>Owens Valley Solar Array</i> . Observations of microwave emission at 6.6 GHz corresponds to the electron gyrofrequency for a 2,400 G magnetic field. (Fletcher et al. 2011 & Qiu et al. 2009)	6
4	Light curves of the M3.5 solar flare SOL2010-06-12 from the GOES 0.5-4 & 1-8 Å channels representing the soft X-Ray emission, the RHESSI 25-50 keV channel, representing the hard X-Ray emission and the SDO/EVE 1-70 & 260 Å channels, representing the extreme UV emission. There is a peak at around 00:55 in the Hard X-Ray (HXR) emission, which is in accordance with the Neupert effect, after which there are four subsequent peaks beginning with the shortest wavelength 0.5-4 Å peaking at 00:57 through to the 260 Å measurements peaking at 01:00. These four sequential peaks represent the gradual cooling of the hot, thermally emitting loop-top plasma.	9
5	Instrument lifetimes with number of sunspots per month over-plotted. Central sunspot peak corresponds to Solar Cycle 24. The \approx 9 year time range highlighted in grey was used for this study, beginning 2010-Apr-30 and ending 2019-May-30. The green highlighted range represents the 314 day period in which all instruments observed simultaneously between 2013-Jul-17 and 2014-May-27.	11

6	A full outer join of two tables keeps all records from both tables in the output. Rows in the two tables which can be matched using a specified parameter(s) are output in the same row. The output table will have all columns present in the two original tables. Figure not to scale.	12
7	Example showing the structure of a time interval list. This is a list containing tuples, containing the start and end times of some time interval. This structure is used for the "non_saa", "non_eclipse" and "observed_times" lists.	15
8	<i>Non-SAA</i> and <i>Non-Eclipse</i> represent lists of tuples describing the start and end times during which the instrument is not in SAA and eclipse respectively. Neither one of these lists can be used on its own to determine if an instrument has an unobstructed view of the Sun, therefore the intersection of these two time ranges must be used for this purpose. This intersection is depicted here as <i>Observing</i> ; a list of tuples describing the start and end times during which the instrument has an unobstructed view of the Sun.	15
9	Bar chart illustrating the distribution of solar flares, categorized by the number of instruments that observed them. Note that a total of 1,737 flares exist in the flare list created in this study between the dates 2013-Jul-17 and 2014-May-27; the period in which all eight instruments were observing the Sun.	20
10	UpSet plot showing the intersection of sets of flares observed by each instrument. This plot is limited to subsets with more than 200 occurrences. From this plot, we can see that the most common collection of instruments to observe a solar flare is Fermi GBM, RHESSI and MEGS-A. It is also possible to see that Fermi GBM, RHESSI, MEGS-A and XRT all observed many more flares than the rest of the instruments. This is due to their FOV and duty cycles, as described in Table 4	21
11	UpSet plot showing the intersection of sets of flares observed by each instrument for flares observed by seven or eight instruments simultaneously.	22
12	Box plots describing the distribution in flare length for flares of GOES class B, C, M and X. A general trend of increasing flare duration with respect to increasing peak soft X-ray flux is seen with an average flare duration for all flares of $\simeq 23$ min.	24
13	Light curves as measured by the GOES X-Ray Sensor, RHESSI and Fermi GBM of the newly discovered well-observed flare, SOL2013-11-09.	26
14	Images captured in different wavelengths by the Atmospheric Imaging Assembly onboard SDO of the newly discovered well-observed flare, SOL2013-11-09.	27
15	All possible overlaps between two lists of intervals, displayed on a number-line.	ii

16	Two examples of overlapping intervals, defined as the range in which $A_{start} <= B_{end}$ and $B_{start} <= A_{end}$	ii
17	Visual representation of the step-wise motion of the two pointers through the two lists of intervals, A and B . Iteration continues until either list A or list B is exhausted.	iii
18	(<i>Top</i>) GOES, RHESSI and Fermi GBM light curves for M2.0 flare, SOL2010-06-12. Despite measuring a significant peak in hard X-Ray flux at 25-20 keV, this flare was not flagged as a flare by RHESSI. Fermi GBM observations made in the same energy band confirm the presence of a hard X-Ray peak. (<i>Bottom</i>) GOES, RHESSI and Fermi GBM light curves for M3.5 flare, SOL2014-01-28. Despite measuring a significant peak in hard X-Ray flux at 25-20 keV, this flare was not flagged as a flare by RHESSI. RHESSI data drops out at 15:27 as the instrument becomes occulted by the Earth. Fermi GBM was not observing the Sun during this flare, most likely as a result of eclipse due to the low variability in measurements.	iv

List of Tables

1	The GOES class of solar flares is based on their peak flux in soft X-rays measured by GOES.	2
2	Information about each of the eight instruments included in this study. <i>%FOV</i> denotes the instruments view as a percentage of the entire Sun (full disk). <i>Orbit</i> describes the orbit of the satellite on which the instrument is located. <i>Cadence</i> is the frequency at which the instrument can make observations. <i>Wavelength</i> is the general wavelength range the instrument observes in. <i>Observation Type</i> is the type of observation each instrument makes in their respective wavelength.	8
3	Class distribution of flares observed by each instrument between 30/04/2010 and 30/05/2019 based on the associated timing and pointing metadata. Success rate is calculated as the percentage of total flares observed by each instrument during its operational lifetime.	19
4	Estimates for the percentage of flares observed by a particular instrument as a product of their duty cycle and field of view. For instruments observing sub-full disk, the estimated success rate assumes a random pointing of the instrument. Based on the flare catalogue described in this report, the actual percentage of flares observed by each instrument during the period beginning 2010-Apr-30 and ending 2019-May-30 is calculated. <i>Lenient Measured Success Rate</i> imposes no restriction on the total fraction an instrument may have observed a given flare while strict measured success rate requires the instrument to have observed more than 50% of the flare to be considered "observed". Duty cycles and field-of-view estimations acquired from Milligan and Ireland (2018).	23
5	Solar flares which have been simultaneously observed by RHESSI, SDO/EVE MEGS-A, SDO/EVE MEGS-B, Hinode/EIS, Hinode/SOT, Hinode/XRT, IRIS and Fermi GBM.	25
6	The Mount-Wilson classification is used to describe active regions on the Sun. δ active regions are the most common region to observe solar flares. Adapted from He et al. (2021).	i

Acronyms

CME Coronal Mass Ejection. 2

EUV Extreme Ultraviolet. 6, 9, 10, 16

Fermi GBM *Fermi Gamma-ray Burst Monitor.* iv, 2, 11, 14–16, 19, 20, 22–24, 28, 29

FOV Field of View. 8, 10, 13, 14, 16–20, 22, 24

GOES *Geostationary Observational Environmental Satellite.* i, iv, 2, 12, 13, 24, 29

HEK *Heliophysics Events Knowledgebase.* i, 12, 13, 24, 29

Hinode/EIS *Hinode/EUV Imaging Spectrometer.* 17

Hinode/SOT *Hinode/Solar Optical Telescope.* 17, 18, 24, 28

Hinode/XRT *Hinode/X-Ray Telescope.* 18–20, 24, 28, 29

HMI *Solar Dynamics Observatory/Helioseismic and Magnetic Imager.* 10

HXR Hard X-Ray. iv, 1, 5–7, 9–11, 13, 14, 19, 25

IRIS *Interface Region Imaging Spectrograph.* 1, 12, 18, 21, 24, 29

RHESSI *Reuven Ramaty High Energy Solar Spectroscopic Imager.* iv, 1, 9, 11, 13, 14, 16, 19, 20, 22–24, 28, 29

SAA South Atlantic Anomaly. ii, iv, 7, 11, 13–16, 19, 23, 24

SDO *Solar Dynamics Observatory.* 1, 10, 16–18

SDO/AIA *Solar Dynamics Observatory/Atmospheric Imaging Assembly.* 12, 25

SDO/EVE MEGS-A *Solar Dynamics Observatory/Extreme ultraviolet Variability Experiment, Multiple EUV Grating Spectrograph A.* 12, 16, 19, 20, 23, 29

SDO/EVE MEGS-B *Solar Dynamics Observatory/Extreme ultraviolet Variability Experiment, Multiple EUV Grating Spectrograph B.* 16, 19, 23

SXR Soft X-Ray. 2, 6, 7, 9, 10, 12, 13, 18, 25

1 Introduction

A vast number of unknown mechanisms drive some of the most energetic events in our solar system, making the study of solar flares a highly valuable area of solar research. Solar flare research is not only important from a space weather perspective, but it also provides an opportunity to improve our understanding of magnetic field interactions, energy release mechanisms, plasma dynamics and stellar processes in some of their most extreme forms. Many instruments, both space and ground based, observe solar flares, collecting imaging, photometric and spectroscopic data from these events. These instruments observe the Sun over the entire electromagnetic spectrum, allowing for the investigation into different layers of the Sun and subsequently, the mechanisms that drive solar flares. Multi-wavelength observations of flares allow for a more complete picture of where the energy is generated, how it is transported and where it ends up throughout the duration of a flare. Filling in gaps in our observed wavelength spectrum allows for "missing energy" to be accounted for, resulting in a more complete understanding of a solar flare's energy budget.

Due to the necessity for multi-instrument observations, data is inevitably scattered across multiple locations. This makes the tracking of which instrument observed which flare significantly more difficult, creating the need for a centralised catalogue of solar flares and each instrument which may have observed them. This would vastly reduce the amount of time taken to find solar flares with a wide range of observed wavelengths as it proves very difficult to accurately coordinate all solar instruments to observe a given solar flare. This is due to the uncertainty in solar flare prediction, the observing schedules in place for these instruments, competing science goals and even coordination between time zones.

When multi-instrument observations of solar flares are made by chance or by coordinated effort, the resulting data receives considerable attention. One example is the 2014-Mar-29, X-class flare observed by *Reuven Ramaty High Energy Solar Spectroscopic Imager* (RHESSI), *Solar Dynamics Observatory* (SDO), *Interface Region Imaging Spectrograph* (IRIS), Hinode and the National Solar Observatory's Dunn Solar Telescope located at Sacramento (Bridgman, 2023). As a result of this wealth of wavelength information, it has been possible to investigate the origin and source of infrared continuum enhancement (Kleint et al. 2016; Simões et al. 2017), the importance of electron beams in driving chromospheric evaporation (Battaglia et al., 2015) and the processes involved in filament eruptions (Woods et al., 2018), amongst other things. Additionally, the first X-class flare of Solar Cycle 24 was simultaneously observed by multiple instruments, allowing Milligan et al. (2014) to investigate the radiated energy budget from chromospheric plasma and Farris and McAteer (2020) to investigate the relationship between HXR flare emission and oscillations in the chromosphere. Multi-wavelength observations of

Class	Flux (W/m ²)
X	$> 10^{-4}$
M	10^{-5}
C	10^{-6}
B	10^{-7}
A	$< 10^{-8}$

Table 1: The GOES class of solar flares is based on their peak flux in soft X-rays measured by GOES.

solar flares allow for a more complete picture of the overall radiative energy budget of a flare, meaning that a well-observed flare is far more valuable than the sum of its parts.

In this study, the effectiveness of eight instruments in co-observing solar flares is presented by retrospectively cross-referencing flare locations and times with the observation metadata recorded by flare observing instruments. The eight instruments selected for this study are as follows, the *Ramaty High Energy Solar Spectroscopic Imager* (RHESSI: Lin et al. 2002), the *Multiple EUV Grating Spectrograph* (MEGS: Crotser et al. 2004) -A and -B components of EVE (Woods et al. 2012), the *EUV Imaging Spectrometer* (EIS: Culhane et al. 2007), the *Solar Optical Telescope* (SOT: Tsuneta et al. 2008), the *X-Ray Telescope* (XRT: Golub et al. 2007), the *Interface Region Imaging Spectrometer* (IRIS: Pontieu et al. 2014) and the *Fermi Gamma Ray Burst Monitor* (Fermi GBM: Meegan et al. 2009). The first seven of these instruments (all but *Fermi Gamma-ray Burst Monitor* (Fermi GBM)) have previously been investigated by Milligan and Ireland (2018), allowing for the comparison of results and some improvements; filling in time gaps¹ in the flare list as well as the expansion of instrument consideration.

1.1 Background

Solar flares are dramatic releases of magnetic energy transmitted in the form of intense bursts of radiation, often occurring in regions called sunspots. As a result of many different processes, flares emit radiation in all wavelengths and are often accompanied by **Coronal Mass Ejections (CMEs)**; large ejections of coronal plasma as well as magnetic field. While flares often vary in terms of the amount of radiation emitted in each wavelength range, the **Soft X-Ray (SXR)** emission from these events are far much more ubiquitous and is therefore used to classify the magnitude of a flare. The "size" of a solar flare is described using the **SXR** flux at $1 - 8 \text{ \AA}$, as measured by **GOES** and is classified into X, M, C, B and A flares; **Table 1**. Each flare is assigned a **GOES** class letter along with an appended number where an M2.0 flare emits twice the peak **SXR** flux compared to an M1.0 flare. Classes A through M have numbers appended between 1.0 = < and < 10.0 while X-class flares can be classed above 10.0; the largest flare ever recorded by **GOES** was an X45 (Hudson et al., 2023). The **GOES** series of satellites are used due to their continuous observations of the Sun since 1975, providing the largest and most

¹October – December 2012; July – November 2013; May 2014; February 2015; March and June 2016.

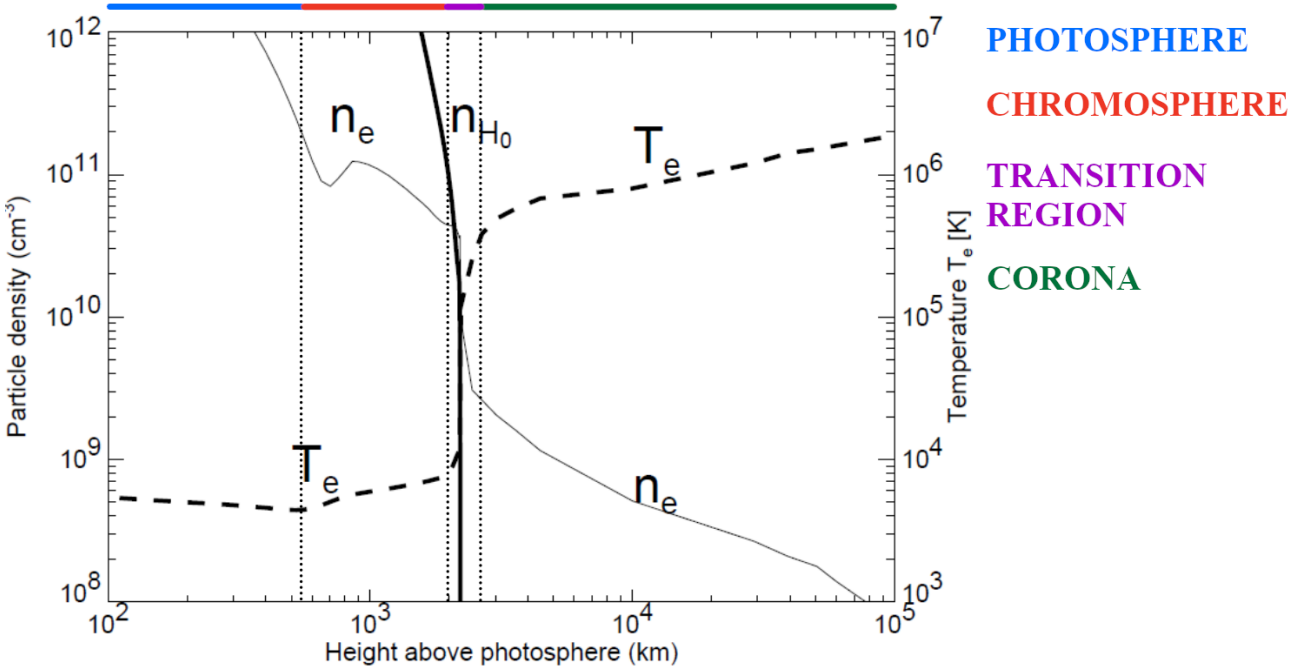


Figure 1: A plot describing the temperature and density of the outer layers of the Sun; the photosphere, chromosphere, transition region and the corona. T_e represents the plasma temperature, n_e is the electron density and N_H is the density of neutral Hydrogen. (Aschwanden, 2005)

consistent record of solar flares on which to build such a flare classification system.

1.1.1 The Photosphere

The photosphere is the deepest part of the Sun we can observe, beyond which the solar plasma becomes opaque. It has a thickness of about 500 km and a temperature of around 4,400 and 6,600 K (Williams, 2022) which counter intuitively is the coolest layer of the Sun. As can be seen in **Figure 1**, the photosphere overall is relatively dense compared to the chromosphere and corona with its density increasing toward the core. The photosphere is home to sunspots where the magnetic field strength increases from ~ 100 G in quiet-Sun regions to $\sim 2,000$ G (Wiegemann et al., 2014).

1.1.2 The Chromosphere

The lower atmosphere of the Sun is called the chromosphere, with a thickness of around 2,500 km. This layer ranges from 4,400 to $\sim 30,000$ K and it can be seen that its temperature increases relative to the photosphere below it in **Figure 1**. The transition between the photosphere and chromosphere is typically defined as the temperature minimum in traditional 1D model atmospheres but in reality, due to the complexity of the chromosphere, the thickness is much more likely to be varied across the Sun (Williams, 2022). The chromosphere emits predominantly in the H_α spectral line and Calcium K-line. Many phenomena may be observed in the

chromosphere such as periodic oscillations in the 5-7 mHz range ([Judge et al., 2001](#)) and their association with solar flares ([Farris and McAteer, 2020](#)).

1.1.3 The Corona

The corona is the outer layer of the Sun which can be directly observed during total solar eclipses. Temperatures in this region of the solar atmosphere are on the order of 10^6 K, far hotter than the photosphere and chromosphere below it however the density of the corona is much lower, exceeding even the strongest vacuums created on Earth. The source of this increased temperature is an active area of research and has been named the coronal heating problem as this dramatic increase in temperature cannot be explained using thermal heating without violating the second law of thermodynamics. It has been theorised that magnetic reconnection and the presence of non-thermal particles could play an important role in understanding the heating mechanisms, both of which are thought to also play a role in solar flares ([Moortel and Browning, 2015](#)).

1.1.4 Sunspots & Active Regions

Sunspots are dark patches on the Sun with intense magnetic fields which inhibit convection, resulting in a relatively low temperature. The lifetime of a sunspot usually ranges between a few days and a few months, during which the sunspot will expand and contract, with diameters ranging from 10^1 to 10^5 km ([Harris, 2007](#)). The number of sunspots varies on an 11-year cycle called the Solar Cycle and they can be found within active regions; areas of strong, complex magnetic fields. Solar flares are typically found in sunspots and are most commonly found in sunspots within δ active regions².

1.1.5 The Standard Model of a Solar Flare

Figure 2 shows the standard model of a solar flare. The magnetic loops extend up into the corona, the outer atmosphere of the Sun, from points on the chromosphere called footpoints. These magnetic fields, thought to result from convection and the rotation of the Sun, store energy in the corona by twisting, stretching and compressing. This magnetic instability leads to magnetic reconnection, where energy is transferred to heat in the surrounding coronal plasma as well and accelerates electrons to relativistic speeds. These electrons have too much energy to be attributed to thermal heating and are therefore called non-thermal electrons. These accelerated electrons spiral down the magnetic field lines, emitting synchrotron radiation³, and

²These active regions are described in more detail in [Appendix A](#).

³Synchrotron radiation is emitted by the spiral motion of charged particles travelling parallel to magnetic field lines ([Ternov, 1995](#)).

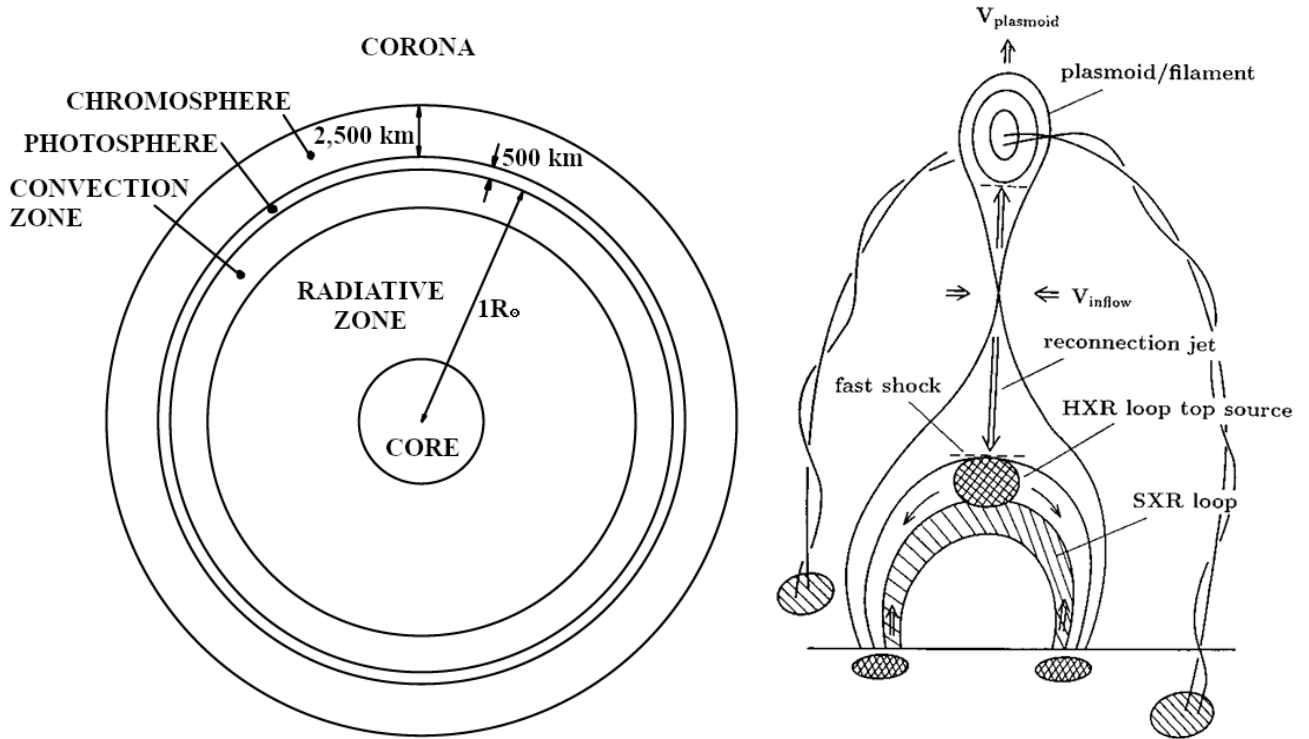


Figure 2: *Left:* Diagram depicting the outer layers of the Sun with layer thicknesses from Williams (2022). *Right:* Cartoon of the standard model of a solar flare. The magnetic loop can be seen extending into the corona, meeting the chromosphere at the footpoints depicted as checkered areas at the ends of the loops. (Shibata, 2015)

bombard the denser chromosphere, resulting in bremsstrahlung radiation⁴, emitting HXRs. This bombardment of the chromosphere results in localised heating in the footpoints, increasing the pressure, leading to chromospheric evaporation and condensation. These processes are named figuratively as these do not describe changes of state, but the motion of the chromospheric plasma. Chromospheric evaporation is the movement of plasma up into the less dense corona while chromospheric evaporation is the subsequent recoiling of the chromosphere in the opposite direction, preserving momentum. Chromospheric evaporation causes hot plasma to rise up into the loop, filling the magnetic loops.

1.2 The Importance of Multi-Wavelength observations

In short, multi-wavelength observations allow for the investigation of the many different interacting mechanisms that occur during a solar flare. To better understand the importance of multi-wavelength observations, we must first take a look at our current understanding of the origin of different wavelengths emitted by a flare. During magnetic reconnection, the acceleration of electrons in the low-density corona results in a small amount of non-thermal emission

⁴Bremsstrahlung radiation is the radiation emitted as a result of the deceleration of a charged particle, when deflected by another charged particle.

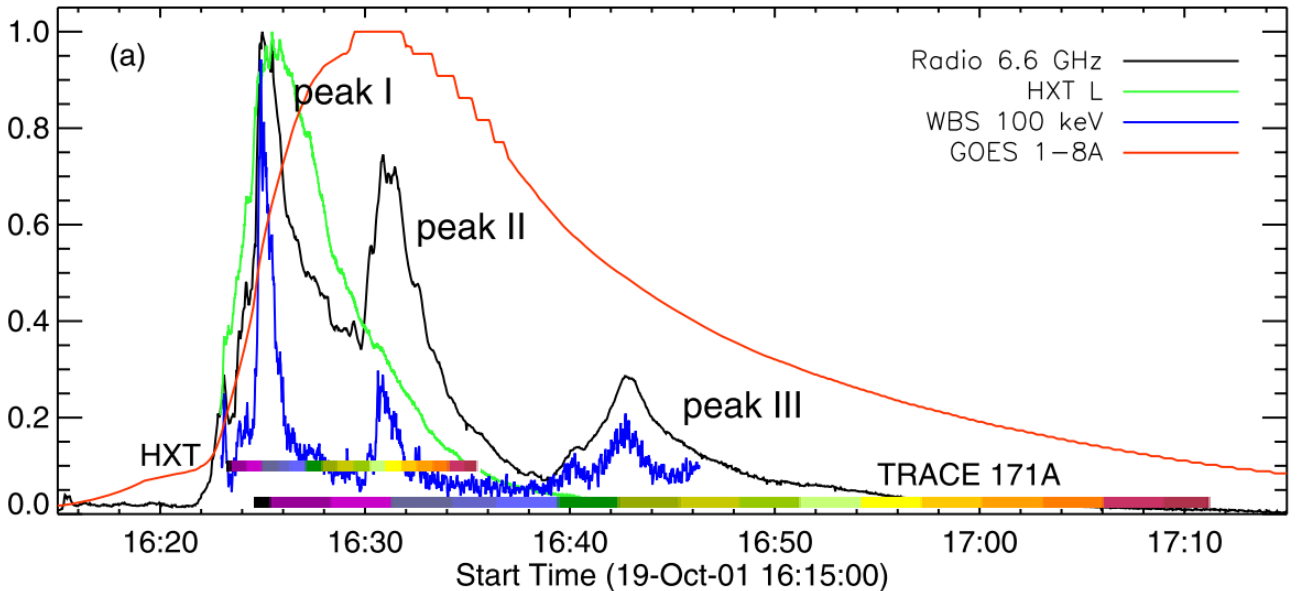


Figure 3: Time evolution of the flare SOL2001-10-19T01:05 (X1.6) in multiple X-ray, EUV, and radio wavelengths. From shortest to longest wavelength: the *blue* line represents the hard X-ray emission as measured by the 100 keV band of the *Yohkoh Wide Band Spectrometer* (WBS); the *green* line represents emission measured by the *Yohkoh Hard X-ray Telescope* (HXT) in its 15-24 keV band; the *red* line represents the soft X-ray emission measured by the 1-8 Å channel of the *GOES X-Ray Sensor* (XRS); and the *black* line represents the shortest-wavelength radio emissions (6.6 GHz) measured by the *Owens Valley Solar Array*. Observations of microwave emission at 6.6 GHz corresponds to the electron gyrofrequency for a 2,400 G magnetic field. (Fletcher et al. 2011 & Qiu et al. 2009)

(HXR bremsstrahlung emission)⁵; localised heating results in thermal emission in the **Extreme Ultraviolet (EUV)** range; and some visible light is emitted through energy transitions of coronal ions. The electrons accelerated by the magnetic reconnection spiral down the magnetic field lines, emitting synchrotron radiation⁶, and bombard the chromosphere, heating the plasma producing thermal emission of UV as well as the non-thermal emission of **HXR**s from non-thermal bremsstrahlung. The plasma evaporated back up into the loop produces thermal emission in the **EUV** range and thermal bremsstrahlung emission in the **SXR**. The photosphere also glows in the visible range at the footpoints however it is not possible for the accelerated electrons to penetrate deep enough through the chromosphere in order to reach the photosphere. The cause of this photospheric brightening is not agreed upon however some theories include illumination of the photosphere by the **HXR** radiation produced in the chromosphere above or perhaps chromospheric condensation results in a compression/heating of the photosphere, causing it to glow.

⁵Loop-top **HXR**s are greatly overpowered by emission from the footpoints. As a result, this radiation is only observable for flares occurring on the solar limb (Sun's outer edge) where the footpoints are obscured but the loop-top remain visible.

⁶The frequency of the emitted synchrotron radiation is the electron gyrofrequency for a particular magnetic field strength.

Throughout the standard model of solar flares, many different mechanisms are interlinked and in order to improve our understanding of these relationships, it is important to have a good understanding of the flare’s radiative energy budget. With multi-wavelength observations of a single flare, the transfer of energy between these mechanisms may be studied and variance between flares can be investigated in more depth. An interesting example of such variances is the Neupert effect which describes the empirical result that for many solar flares the soft X-ray time derivative resembles the hard X-ray time profile. Veronig (2003) found that around 25% of solar flares show strong deviations from the Neupert effect, with increasing thermal emission beyond the end of the HXR emission and suggested that this may be evidence for a prolongation of chromospheric evaporation by thermal conduction. For this example, simultaneous SXR and HXR observations must be made in order to study the relationship between these two emission mechanisms, demonstrating that the simultaneous multi-wavelength observation of a single solar flare is greater than the sum of its individual observations.

Figure 3 presents the multi-wavelength observation of an X1.6 flare. With these data, it is possible to determine the suitability of using the standard model to describe this particular flare. The strong correlation between the black (6.6 GHz) and blue (HXR) lines suggests a direct relationship between these measurements. This may be explained by the non-thermal electrons emitting synchrotron radiation at 6.6GHz as they spiral down the magnetic field lines, impacting the chromosphere and emitting HXR radiation almost instantaneously due to the relativistic velocities of the electrons. The HXR peak (black) occurs before the SXR peak (red), corresponding to the theory that chromospheric evaporation fills the magnetic loop with hot plasma, resulting in the thermal bremsstrahlung emission of SXRs.

1.3 Challenges of Multi-Wavelength Observations

A number of factors result in multi-wavelength observations being difficult to coordinate. To begin with, it is not possible to predict the time and location in which a particular event may occur. Despite knowing that active regions (in particular δ active regions) are the most common areas to observe flares, it is never certain that flares will be observed. Even with perfect flare prediction, observing schedules sometimes prohibit the observation of a newly developed flare-producing region as observation schedules can sometimes be uploaded to the spacecraft weeks in advance. Additionally, with competing science goals for the solar observing instruments, it is not possible to observe all promising active regions in search of flares. As shown in **Table 2**, the orbit of these instruments can sometimes prohibit the observation of a particular flare due to eclipse and South Atlantic Anomaly (SAA)⁷. Additionally, an instrument’s orbit may dictate the cadence with which it makes observations as the rate at which data can be transmitted

⁷Further explanation of SAA in **Section 2.3.1**.

Instrument	%FOV	Orbit	Cadence	Wavelength	Observation Type
RHESSI	100%	Low Earth Orbit	4 sec	0.003-17 MeV	Imaging Spectrometer
Fermi GBM	100%	Low Earth Orbit	4 sec	0.006-0.8 MeV	Spectrograph
SDO/EVE MEGS-A	100%	Geosynchronous	10 sec	5-37 nm	Spectrograph
SDO/EVE MEGS-B	100%	Geosynchronous	10 sec	35-105 nm	Spectrograph
Hinode/EIS	2-25%	Sun-synchronous	<1/10 sec	18-29 nm	Imaging Spectrometer
Hinode/SOT	1-17%	Sun-synchronous	10 sec	450 nm	Imager
Hinode/XRT	25-100%	Sun-synchronous	5/10 sec	1.3-500 nm	Imager
IRIS	0.5-3%	Sun-synchronous	1 sec	133.2-283.5 nm	Imager & Spectrograph

Table 2: Information about each of the eight instruments included in this study. *%FOV* denotes the instruments view as a percentage of the entire Sun (full disk). *Orbit* describes the orbit of the satellite on which the instrument is located. *Cadence* is the frequency at which the instrument can make observations. *Wavelength* is the general wavelength range the instrument observes in. *Observation Type* is the type of observation each instrument makes in their respective wavelength.

back to Earth depends on the satellite’s line of sight to a ground station. Instruments placed in low Earth orbit will only pass a particular ground station once per orbit, meaning that all data recorded during this orbit must be transmitted in the short period of time in which the ground station is in view. Instruments in geostationary or geosynchronous orbits are in view of a ground station at all times, allowing for a higher total volume of observation data. Furthermore, each instrument has a different **Field of View (FOV)**, meaning that not only do observations need to be made simultaneously, they also must be pointed in the same direction. Observing a flare with instruments using rasterisation is even more difficult as the flare must align in space and time with the moving rasterisation window making successful rasters of flares exceedingly rare⁸ (Milligan, 2015).

It may seem sensible to place all solar observing instruments in geostationary orbit and have a 100% **FOV** however, each of these parameters have trade-offs. For example, it is more expensive to place an instrument into geostationary orbit compared to low Earth orbit, observations made with a smaller **FOV** yield improved spatial resolution and observations using rasterisation can provide improved spectral resolution. Designing an instrument and planning its mission will always include compromises between various science goals as well as budget constraints, it is then important to extract as much value as possible from the tools provided. Despite these challenges, flare-specific observing runs can improve observation coordination; the *Max Millennium Program of Solar Flare Research*^{9,10} initially coordinated ground-based observations with

⁸Rasterisation is the systematic movement of a telescope across a region, capturing images at each position, discussed further in **Section 2.3.4**.

⁹Max Millennium Program of Research: https://solar.physics.montana.edu/max_millennium/proposal.shtml#:~:text=The%20primary%20goal%20of%20the,the%20last%20two%20sunspot%20cycles.

¹⁰Max Millennium Observing Plans: https://solar.physics.montana.edu/max_millennium/ops/

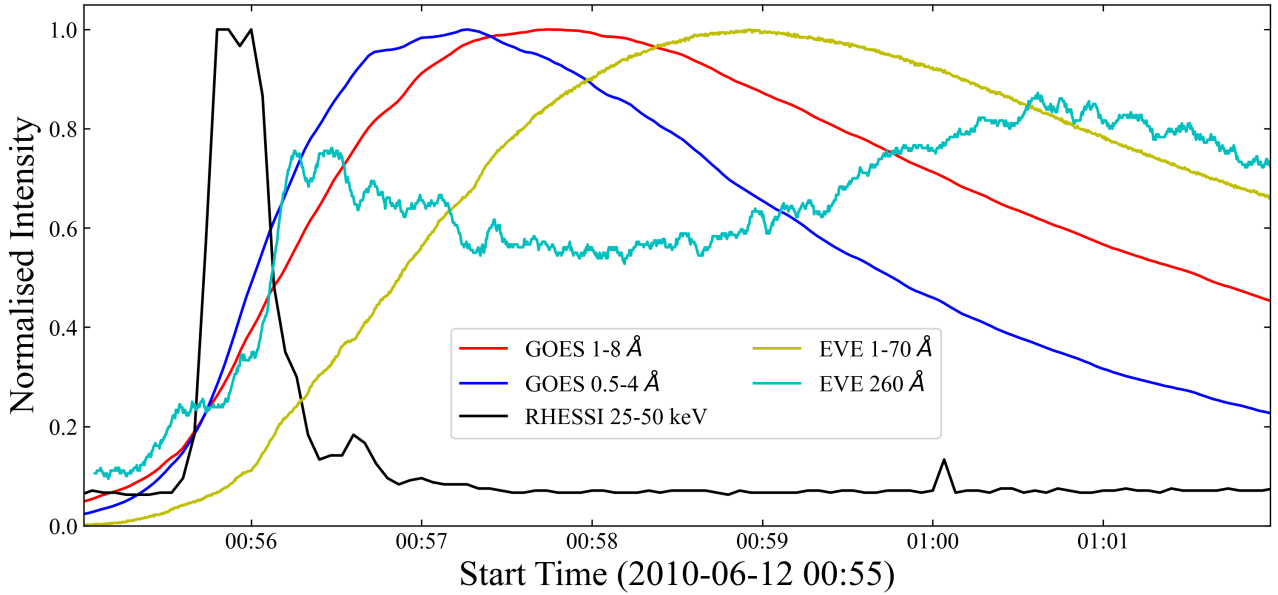


Figure 4: Light curves of the M3.5 solar flare SOL2010-06-12 from the GOES 0.5-4 & 1-8 Å channels representing the soft X-Ray emission, the RHESSI 25-50 keV channel, representing the hard X-Ray emission and the SDO/EVE 1-70 & 260 Å channels, representing the extreme UV emission. There is a peak at around 00:55 in the HXR emission, which is in accordance with the Neupert effect, after which there are four subsequent peaks beginning with the shortest wavelength 0.5-4 Å peaking at 00:57 through to the 260 Å measurements peaking at 01:00. These four sequential peaks represent the gradual cooling of the hot, thermally emitting loop-top plasma.

observations made by **RHESSI** with the broad objective of improving our understanding of particle acceleration within solar flares. As **RHESSI** makes full disk observations, the coordination effort involved the definition of a ground-based observatory campaign and the documentation and evaluation of current solar conditions. There are currently 8 space based and 47 ground based collaborating observatories with current scientific objectives including the role of high energy particles in energy release and energy transport, exploration of particle acceleration mechanisms, flare energy transport mechanisms and the identification of potentially hazardous flares.

1.4 Outstanding Questions in Solar Flare Physics

There are a number of outstanding questions surrounding the physics of solar flares and the goal for a catalogue of flares and their associated co-observations is to aid in the investigation of these outstanding questions. The heating and cooling process within a solar flare can be investigated using **SXR** and **EUV** observations; **Figure 4**, magnetic field structure, its spatial and temporal relationship with non-thermal electrons and particle acceleration mechanisms may be studied

observing.shtml

through a combination of **EUV** observations and magnetograms¹¹. Additionally, it is possible to investigate the magnetic field structure at the beginning of a solar flare, allowing for research into what triggers magnetic reconnection and potentially the discovery of flare precursors using a combination of magnetograms and **SXR** observations. During a solar flare, photospheric emission can be observed along the footpoints of the flare; in order to investigate this emission, flares with simultaneous **HXR** and visible observations must be studied. Finally, the radiative energy budget of a solar flare is not fully understood with outstanding questions surrounding the path energy takes throughout the duration of a flare, the energy transfer mechanisms and the final destination of this energy. In order to study flare energy budgets, observations in as many wavelengths as possible must be used.

2 Method

The aim of this study was to create a catalogue of solar flares and identify any instruments which may have observed them. This creates a quick and easy way to obtain a list of flares with such simultaneous observations, greatly reducing the amount of time required to find the data as well as highlighting observations with significant research potential.

2.1 Initial Parameters

Initially, some decisions must be made on the instruments and time range to include in this study. **Table 2** describes various properties of the eight instruments included in this study:

1. *Ramaty High Energy Solar Spectroscopic Imager* (RHESSI)
2. *Solar Dynamics Observatory/Extreme ultraviolet Variability Experiment, Multiple EUV Grating Spectrograph A* (MEGS-A)
3. *Solar Dynamics Observatory/Extreme ultraviolet Variability Experiment, Multiple EUV Grating Spectrograph B* (MEGS-B)
4. *Hinode/EUV Imaging Spectrometer* (EIS)
5. *Hinode/Solar Optical Telescope* (SOT)
6. *Hinode/X-Ray Telescope* (XRT)
7. *Interface Region Imaging Spectrometer* (IRIS)
8. *Fermi Gamma Ray Burst Monitor* (Fermi GBM)

¹¹Whilst an instrument capable of observing magnetograms has not been included in this study, the, as a result of its 100% **FOV** and geosynchronous orbit, it can be assumed that any observations made by the instruments included in this study during the lifetime of **SDO** will have simultaneous *Solar Dynamics Observatory/Helioseismic and Magnetic Imager* (**HMI**) observations.

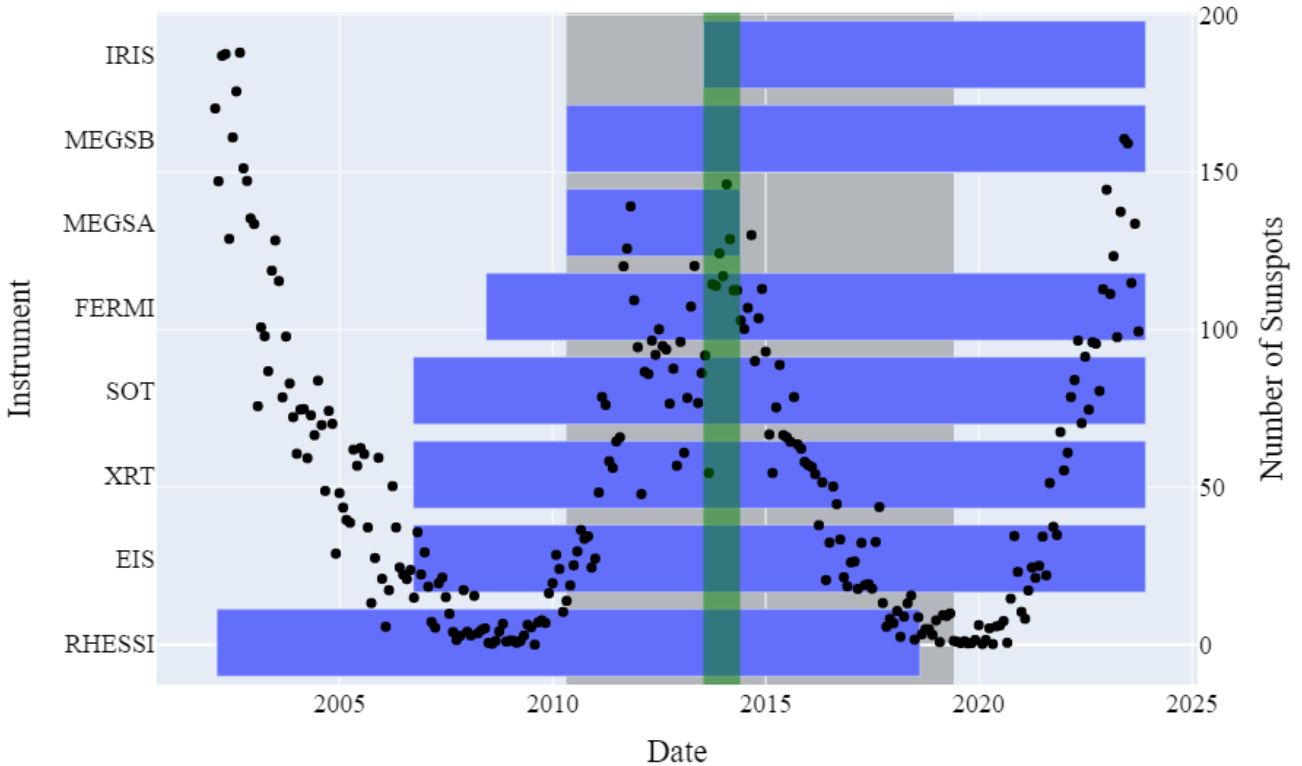


Figure 5: Instrument lifetimes with number of sunspots per month over-plotted. Central sunspot peak corresponds to Solar Cycle 24. The ≈ 9 year time range highlighted in grey was used for this study, beginning 2010-Apr-30 and ending 2019-May-30. The green highlighted range represents the 314 day period in which all instruments observed simultaneously between 2013-Jul-17 and 2014-May-27.

The first seven of these instruments were included in a previous study by Milligan and Ireland (2018), allowing for comparison of results. Additionally, this study suffered from several months of missing data¹² at the time, meaning some overlap in investigation scope is advantageous. An additional instrument, **Fermi GBM**, was added to broaden the initial investigation and was chosen as it observes in the **HXR** to γ -rays range, meaning that it may serve as a backup in this wavelength range. **Fermi GBM** is not a solar instrument, however in its search for gamma-ray bursts, it uses a detector which makes constant observations of the Sun to subtract this contribution from its other detectors. Subsequently, **RHESSI** observations are preferred over observations made by **Fermi GBM** however, due to **RHESSI**'s low Earth orbit, it is likely to miss observations of solar flares as a result of eclipse and **SAA**. For flares not observed by **RHESSI**, the addition of **Fermi GBM** in this study allows for the possibility that these flares are observed in the **HXR** to γ -ray range.

Selecting a time range for this study incorporated a number of factors. For a given time range, it is important that a majority of the instruments selected for this study are active and there are a good number of solar flares to observe. **Figure 5** displays the mission duration for each for the instruments. Over-plotted is the number of sunspots per month, indicating the Sun's activity

¹²October – December 2012; July – November 2013; May 2014; February 2015; March and June 2016.

and therefore abundance of solar flares. An appropriate time range beginning 2010-Apr-30 and ending 2019-May-30 was selected, encompassing a period of high solar activity (Solar Cycle 24) and good instrument coverage. It is important to note at this time that there is a short period between the launch of **IRIS** and the CCD failure of *Solar Dynamics Observatory/Extreme ultraviolet Variability Experiment, Multiple EUV Grating Spectrograph A* (SDO/EVE MEGS-A) where all instruments observe the Sun simultaneously. This greatly reduces the likelihood a solar flare is observed by all eight instruments simultaneously and should be considered when scrutinising the performance of multi-instrument observations. During the time range highlighted in grey in **Figure 5**, 14,458 distinct solar flares were recorded in the **GOES** flare list¹³ and **HEK** register flare list¹⁴.

2.2 Combining Flare Lists

2.2.1 Selecting Existing Flare Lists

In order to create a catalogue of solar flares and any instruments which may have observed them, it is important to create a comprehensive list of solar flares that occurred on the Sun during the time range considered in this study. This list was created by joining two existing flare lists, the first of which is the **GOES** flare list. **GOES** is a series of weather satellites which have continuously observed the Sun since 1975 and as a result, the peak in their **SXR** measurements have become the widely accepted definition of a solar flare. The **HEK** register was developed to help with browsing *Solar Dynamics Observatory/Atmospheric Imaging Assembly* (SDO/AIA) data and is the second of the two joined flare lists. The **HEK** combines observations made by multiple different instruments to construct its flare list, meaning that in some cases, flares are included in the **HEK** register flare list that are not present in the **GOES** flare list. In previous attempts at creating catalogues of multi-instrument observations, the **GOES** and **HEK** flare lists have been used to great effect, suggesting that the joining of these lists would be a strong basis for subsequent analysis (Sadykov et al., 2017).

¹³<https://umbra.nascom.nasa.gov/goes/fits/>

¹⁴<https://www.lmsal.com/isolsearch>

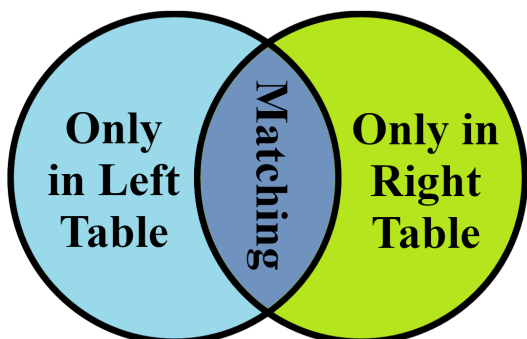


Figure 6: A full outer join of two tables keeps all records from both tables in the output. Rows in the two tables which can be matched using a specified parameter(s) are output in the same row. The output table will have all columns present in the two original tables. Figure not to scale.

2.2.2 Joining Existing Flare Lists

The selected flare lists are joined on the flare peak time¹⁵ using a full outer join (described by **Figure 6**). The table resulting from this join contains all columns present in both tables, meaning the "flare_start"¹⁶, "flare_end"¹⁷ and "class"¹⁸ columns are duplicated, containing almost identical information sourcing from the two original flare lists. For the same flare, the **GOES** flare list and the **HEK** register flare list sometimes record these duplicated columns with very minor differences. These differences in the values stem from the instrument responsible for calculating them. Even within the **GOES** series of satellites, two different spacecraft will have slight differences in the **SXR** flux measurements made during the same solar flare. These small flux differences can not only result in differences in **GOES** class, but also flare start, peak and end times as these are all determined using the **SXR** flux. To handle these cases, for each flare present in both the **GOES** flare list and the **HEK** register flare list, the earliest "flare_start", latest "flare_end" and largest "class" are used.

2.3 Determining an Instrument's Observation of a Solar Flare

For each solar flare present in this newly constructed flare list, it must be determined whether each of the eight instruments made an observation during the event. As a result of the parameters described in **Table 2**, each instrument must employ a specialised approach, however the two main questions remain the same:

1. Could the instrument see the Sun at the time of the flare?
2. Did the flare occur within the instrument's **FOV**?

A flare is only observed by an instrument when the answer to each of these questions is yes.

2.3.1 Reuven Ramaty High Energy Solar Spectroscopic Imager

RHESSI is an imaging spectrometer, observing the full disk in the **HXR** to γ -ray range which was launched 2002-Feb-15 and ended 2018-Aug-16. The instrument is in low Earth orbit meaning that answering the question of "could the instrument see the Sun at the time of the flare" is particularly important. For any instrument in low Earth orbit, its view of the Sun will be eclipsed by the Earth once every orbit. In addition, these instruments pass through a region of the Earth's magnetic field named the South Atlantic Anomaly (**SAA**). This can be

¹⁵Flare peak: The minute in which the peak **SXR** flux measurement is made.

¹⁶Flare start: The first minute, in a sequence of 4 minutes, of steep monotonic increase in **SXR** flux.

¹⁷Flare end: The minute in which the **SXR** flux decays to a point halfway between the maximum flux and the pre-flare background level.

¹⁸**GOES** class: A classification system to categorise solar flares based on their intensity using classes A, B, C, M, and X. **Table 1**

thought of as the Bermuda triangle for satellites, a region over South America where the Earth's magnetic field strength is relatively low, allowing for more radiation to penetrate into low Earth orbit. Any observations made by instruments in **SAA** must be discarded and therefore must be considered when confirming the instrument's view of the Sun.

RHESSI records a number of different flags for each observation it makes. These are accessible as Boolean lists with each element representing the flag's state for an individual observation. The two flags of interest are the "SAA_FLAG" and "ECLIPSE_FLAG"; these flags are 1 for observations made in **SAA** or eclipse. Using these Boolean lists, an "observed_flag" can be created with the following logic:

$$\text{observed_flag} = \text{NOT} (\text{saa_flag} \text{ OR } \text{eclipse_flag}) \quad (1)$$

With the "observed_flag" list, it is possible to answer the question of whether **RHESSI** could see the Sun at the time of the flare. A time is associated with each Boolean element in the "observed_flag" list, meaning that the list can be trimmed to the flare start and end times. If any elements of this trimmed Boolean list are 1, **RHESSI** is said to have observed the solar flare.¹⁹ The observed fraction of the flare may be calculated by summing the list and dividing by the total number of elements, providing a better understanding of the amount of data available for a particular observation. This can be further broken down into the observed fractions of the impulsive phase²⁰ and gradual phase²¹ of each flare. The flare peak time can be used to split the Boolean list into these two phases, it is then determined whether the flare was observed during these phases and the observed fraction is calculated. **RHESSI** observes the full disk meaning that if the instrument was observing the Sun at the time of the flare, it will have made an observation of said flare.

2.3.2 Fermi Gamma-Ray Burst Monitor

Fermi GBM is a spectrograph searching for gamma-ray bursts which was launched 2008-Jun-11 and continues to make **HXR** and γ -ray observations to this day. The instrument is placed in a low earth orbit and observes the full disk of the Sun. Due to the similarity in orbit and **FOV** between **RHESSI** and **Fermi GBM**, a very similar approach may be used to determine if a flare is observed.

Similarly to **RHESSI**, eclipse and **SAA** are recorded alongside measurements however, they are not stored in an identical format. Where **RHESSI**'s eclipse and **SAA** flags were recorded in the

¹⁹A minimum on one element of the Boolean list must be 1 for a flare to be "observed" by **RHESSI**. This means that **RHESSI** may have only observed the flare for 4 seconds (**RHESSI**'s minimum observing cadence.)

²⁰The impulsive phase: the period of time between the flare start time and the flare peak time.

²¹The gradual phase: the period of time between the flare peak time and the flare end time.

```
[  

  (start_time_1, end_time_1),  

  (start_time_2, end_time_2),  

  (start_time_3, end_time_3),  

  ...  

]
```

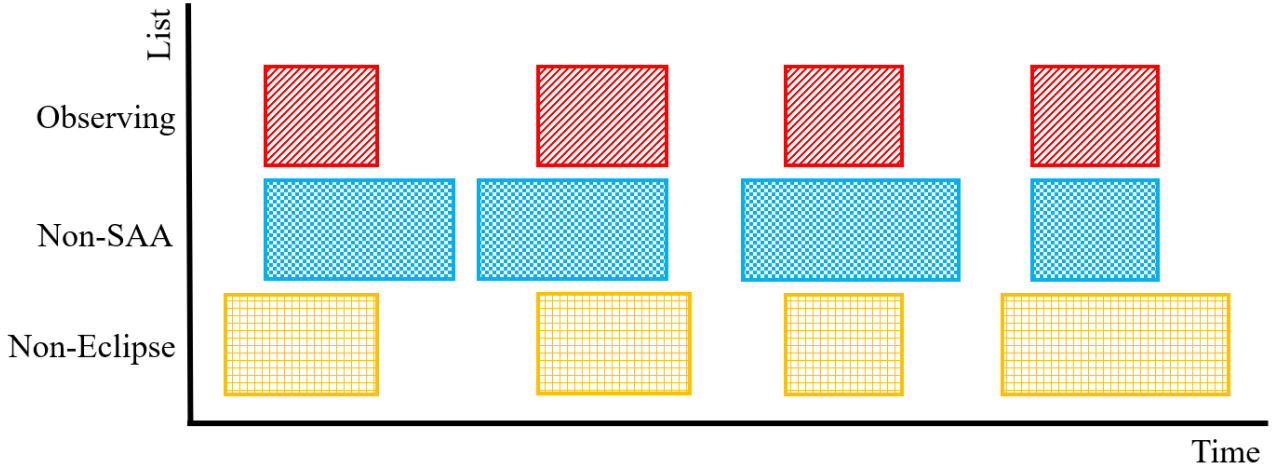


Figure 8: *Non-SAA* and *Non-Eclipse* represent lists of tuples describing the start and end times during which the instrument is not in SAA and eclipse respectively. Neither one of these lists can be used on its own to determine if an instrument has an unobstructed view of the Sun, therefore the intersection of these two time ranges must be used for this purpose. This intersection is depicted here as *Observing*; a list of tuples describing the start and end times during which the instrument has an unobstructed view of the Sun.

form of Boolean lists, Fermi GBM records these events as start and end times of non-eclipse and non-SAA periods.²² These are stored as lists of tuples, the structure of which can be seen in **Figure 7**. As a result, the logic described in **Equation (1)** cannot be used and must be replaced with a more complicated algorithm.

Figure 8 visualises this problem where *Observing* represents the list of tuples that should result from this algorithm. Using the approach described in **Appendix B**, it is possible to determine whether an observation of the flare has been made. Initially, an "observed_times"²³ list of time intervals is created which is the intersection between the "non_saa" and "non_eclipse" lists. Then using the same algorithm, the intersection between this "observed_times" list and the flare start and end times can be found. If this returns no overlapping time ranges, the flare has not been observed; Fermi GBM was either in SAA, eclipse or a combination of both for the entire duration of the flare. On the other hand, if the returned list is not empty, there has been

²²Non-eclipse time ranges and non-SAA time ranges are stored in separate lists, meaning overlap between these two lists is possible.

²³"observed_times" is stored in the same format described in **Figure 7**.

at least one observation made throughout the duration of the flare. In order to calculate the observed fraction of the flare, the difference between the start time and the end time within each tuple is calculated and then summed for the entire list, resulting in the total amount of time for which the instrument was observing the flare. This value divided by the difference between the flare start and flare end times results in the fraction observed. Similarly with **RHESSI**, the fraction of the impulsive and gradual phases of the flare can also be calculated by repeating the above steps but replacing flare end with flare peak (for impulsive phase) and replacing flare start with flare peak (for gradual phase).

As **Fermi GBM** observes the full disk, it is once again a trivial task answering the question of "did the flare occur within the instrument's **FOV**?" - yes.

2.3.3 Solar Dynamics Observatory - Extreme Ultraviolet Variability Experiment

This experiment is home to two instruments included in this study, **SDO/EVE MEGS-A** and *Solar Dynamics Observatory/Extreme ultraviolet Variability Experiment, Multiple EUV Grating Spectrograph B* (**SDO/EVE MEGS-B**). Both instruments are spectrographs making full disk observations in the **EUV** range. The satellite was launched into a geosynchronous orbit on 2010-Apr-30. **SDO/EVE MEGS-A** stopped working on 2014-May-27 while **SDO/EVE MEGS-B** currently remains in service.

Due to **SDO**'s geosynchronous orbit, it is very rare that the instruments will experience an eclipse and transits through **SAA** do not occur. This paired with these instruments full disk observations vastly simplifies the process. For **SDO/EVE MEGS-A**, determining whether a flare has been observed is as simple as determining whether the flare occurred during the instrument's lifetime. While **SDO/EVE MEGS-B** shares similar properties to **SDO/EVE MEGS-A**, an identical approach can not be used. Due to degradation of the detector, **SDO/EVE MEGS-B** is restricted to making three hours of observations per day with extra observations made during energetic/interesting events. The observing times are stored as a .csv online,²⁴ allowing for the time ranges during which the instrument could see the Sun to be extracted. With the observing time ranges extracted, they can be stored in the same format used in **Figure 7**, therefore allowing for the same interval intersection algorithm described in **Appendix B** to be used here. From this point on, it is possible to follow the same steps described in **Section 2.3.2** to determine whether a particular flare has been observed, as well as the observed fraction of the total flare, impulsive and gradual phases.

²⁴http://lasp.colorado.edu/eve/data_access/evewebdata/interactive/megsb_daily_exposure_hours.csv

2.3.4 Hinode - EUV Imaging Spectrometer

The Hinode satellite, launched into a Sun-synchronous orbit on 2006-Sep-26, is home to three instruments, one of which is *Hinode/EUV Imaging Spectrometer* (Hinode/EIS). This instrument is unique as it is able to image the surface of the Sun whilst simultaneously making a spectral observation. Hinode/EIS has two narrow slits (1" & 2" width) and two wide slots (40" & 266" width) giving the instrument a much smaller FOV of 2-25%. Due to these slits and slots, rasterisation is used in order to make observations. Rasterisation is the systematic movement of a telescope across a region, capturing images at each position. Due to this observation method, it is a lot more unlikely for solar flares to be captured using this telescope as the flare has to occur within a very small region of the Sun currently being observed by the instrument.

As Hinode/EIS is in a Sun-synchronous orbit, similarly to the SDO instruments, it is rare that the instrument experiences an eclipse. This means that for this instrument, it is also possible to reduce the question of "could the instrument see the Sun at the time of the flare" to "did the flare occur during the instrument's lifetime".

Determining whether the flare occurred within the instrument's FOV is more complicated for this instrument and requires the use of the pointing information recorded with each observation alongside the FOV in the x and y directions. The flare's position is compared with the metadata associated with each observation and it can be determined whether or not the instrument was pointed at the flare. The fraction of total flare, impulsive phase and gradual phase observed is then calculated in a similar manner to the other instruments; the total time the instrument is pointed at the flare location is divided by the total time of the entire flare, impulsive phase and gradual phase.

2.3.5 Hinode - Solar Optical Telescope

Hinode/Solar Optical Telescope (Hinode/SOT) is the first large optical telescope to be launched into space which images the Sun between 480-650 nm with a FOV between 1-17%. Its Focal Plane Package allows it to produce vector magnetograms, measure Doppler velocities as well as photospheric intensity. As a result of this instrument's rasterisation and format of data, it is difficult to obtain an accurate value for the fraction observed of the entire flare, impulsive phase and gradual phase. As a result, this investigation resorts to a simplistic Boolean value for whether or not Hinode/SOT observed a particular flare. This is determined by finding observations made within the flare duration and determining if the flare occurred within the observation's FOV.

2.3.6 Hinode - X-Ray Telescope

Hinode/X-Ray Telescope (*Hinode/XRT*) takes SXR images in the 0.2-2 keV range with a FOV of 25-100%. With images obtained using this instrument, coronal structures may be investigated with a temperature range of 0.5-10 MK, revealing details of magnetic field structures and their evolution. Similar to *Hinode/SOT*, it is difficult to determine observed fractions and therefore a simplistic Boolean value for whether or not *Hinode/XRT* observed a particular flare is used. Again, this value is determined by checking whether a flare occurred within the FOV of any observations made throughout the duration of the flare.

2.3.7 Interface Region Imaging Spectrograph

Lastly, *IRIS*, launched in 2013-Jul-17, is an ultraviolet imager and spectrograph in a Sun-synchronous orbit still operating today with a 0.5-3% FOV. Determining observed fractions is relatively straightforward for *IRIS* and as a result, a flare is considered observed if, for the observations made by the instrument throughout the duration of the flare, the flare is located within the instrument's FOV. The observed fraction is then calculated through the summation of overlapping time ranges (again, using the algorithm detailed in [Appendix B](#)) between the flare duration and the successful observations made by *IRIS*. Observed fractions of the impulsive and gradual phases are calculated using the same method, replacing the entire flare duration with a shorter time range containing only the impulsive/gradual phase.

3 Results

3.1 Statistics of Multi-Wavelength Observations

During the time period beginning with the launch of *SDO* (2010-Apr-30) and ending around the conclusion of Solar Cycle 24 (2019-May-30), 14,458 flares were recorded in the flare catalogue described in this report. It was found that 98.5% of flares in the flare list described in [Section 2.2](#) were observed by at least one of the eight instruments included in this study. [Table 3](#) forms a summary of the total number of flares observed by each instrument along-side their success rate in observing solar flares. An instrument's success rate was calculated as follows:

$$\text{Success rate} = \left(\frac{\text{Num. Observed Flares}}{\text{Num. Observable Flares}} \right) \times 100 \quad (2)$$

Where:

- Num. Observed Flares = Total number of flares observed by the instrument during the considered time range.

Table 3: Class distribution of flares observed by each instrument between 30/04/2010 and 30/05/2019 based on the associated timing and pointing metadata. Success rate is calculated as the percentage of total flares observed by each instrument during its operational lifetime.

Instrument/Database	B-class	C-class	M-class	X-class	Total	Success rate over 9.1 years ^a
GOES/HEK	6,154	7,537	718	49	14,458	100%
RHESSI	3,901	5,496	553	39	9,989	71%
SDO/EVE MEGS-A ^a	3,197	4,745	428	30	8,400	100%
SDO/EVE MEGS-B	725	1,066	152	13	1,956	14%
Hinode/EIS	478	669	81	11	1,239	9%
Hinode/SOT	636	1,302	201	19	2,158	15%
Hinode/XRT	3,294	4,106	418	35	7,853	54%
IRIS	662	648	89	5	1,404	18%
FERMI GBM	4,611	5,769	593	44	11,017	76%

^aMEGS-A was assumed to have observed all flares between its launch (30/04/2010) and end of life (26/05/2014).

- Num. Observable Flares = Total number of flares that occurred during the instrument's lifetime and within the considered time range.

As expected, it is evident that instruments with a full-disk view of the Sun and a high duty cycle observe significantly more flares than the other instruments, with **RHESSI**, **SDO/EVE MEGS-A**, **Hinode/XRT** and **Fermi GBM** achieving the highest success rates. The remaining instruments achieving a success rate below 20% either had a reduced duty cycle²⁵ and/or a much lower **FOV**.

[Milligan and Ireland \(2018\)](#) completed an identical analysis for a time period of 6.5 years, producing similar values for success rate for all instruments except **RHESSI** with a success rate of 58%. As seen in **Table 3**, the success rate calculated in this study is 71% during the 9.1 year period. This contradiction is most likely to be as a result of a differing approach to classifying a flare as "observed". The method described in this report (**Section 2.3.1**) regards any observations made outside eclipse and **SAA** as a valid observation of the flare while in [Milligan and Ireland \(2018\)](#), the **RHESSI** flare flag is used. These flags are applied using only the data recorded by **RHESSI** and as a result, a significant peak in **HXR** flux must be recorded in order to be marked as a flare. Despite this, there are some cases where even large M-Class solar flares are observed (and are reflected as large peaks in the observations) but are not flagged

²⁵**SDO/EVE MEGS-B** makes full-disk observations however, due to sensor degradation, it is restricted to 3 hours of observation per day, resulting in a lower success rate.

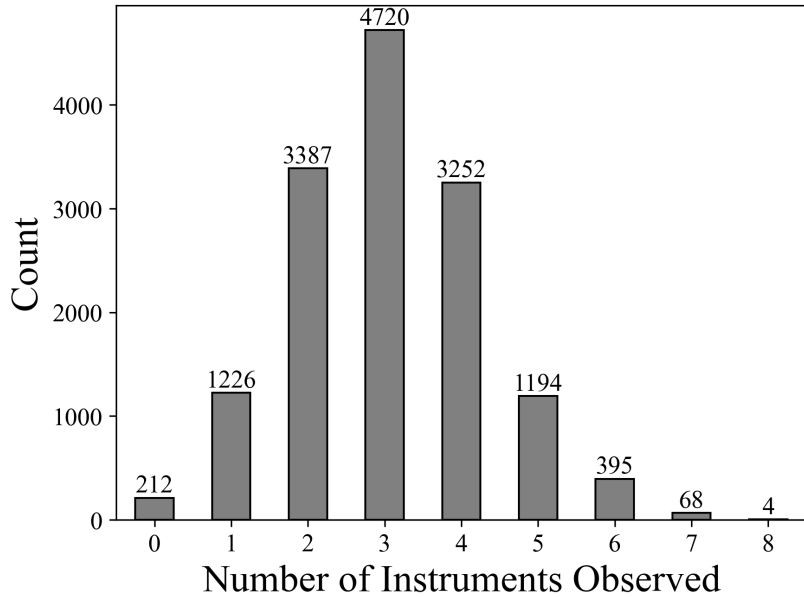


Figure 9: Bar chart illustrating the distribution of solar flares, categorized by the number of instruments that observed them. Note that a total of 1,737 flares exist in the flare list created in this study between the dates 2013-Jul-17 and 2014-May-27; the period in which all eight instruments were observing the Sun.

as flares by RHESSI²⁶. For this reason, the method described in [Section 2.3.1](#) has been used.

[Figure 9](#) visualises the number of flares simultaneously observed by different numbers of instruments between the dates 2010-Apr-30 and 2019-May-30. From this figure, we can see that the most common number of instruments to observe a particular solar flare is three. The reason for this is attributed to a range of factors, FOV, duty cycle, instrument lifetime and the solar activity during the instrument’s lifetime. Furthermore, we can deduce that a large number of flares have broad multi-instrument observations as 1,194, 395 and 68 flares were simultaneously observed by a combination of five, six and seven instruments respectively. A total of four flares were observed by all eight instruments simultaneously out of a total of 1,737 flares that occurred between the dates 17/07/2013 and 27/05/2014; the period in which all eight instruments were observing the Sun.

A deeper understanding of the different combinations of instruments used to simultaneously observe these solar flares can be gained through the use of the UpSet plot in [Figure 10](#) ([Lex et al., 2014](#)). Here, we can see the different subsets of instruments and the number of events which have been observed with each combination. The most common combination of instruments to observe a given event is SDO/EVE MEGS-A, RHESSI and Fermi GBM followed closely with the same set of instruments plus Hinode/XRT. As discussed previously, these instruments all have a high FOV and duty cycle, meaning that it is unsurprising that these combinations of instruments were most effective in co-observing flares. The total number of flares observed by each instrument is given as the horizontal bar chart in the bottom left of the figure. This visualises the benefit of a large FOV and high duty cycle if the sole objective

²⁶See [Appendix C](#) for examples of M-Class solar flares collected in this study where RHESSI observed the event but failed to flag the event as a flare.

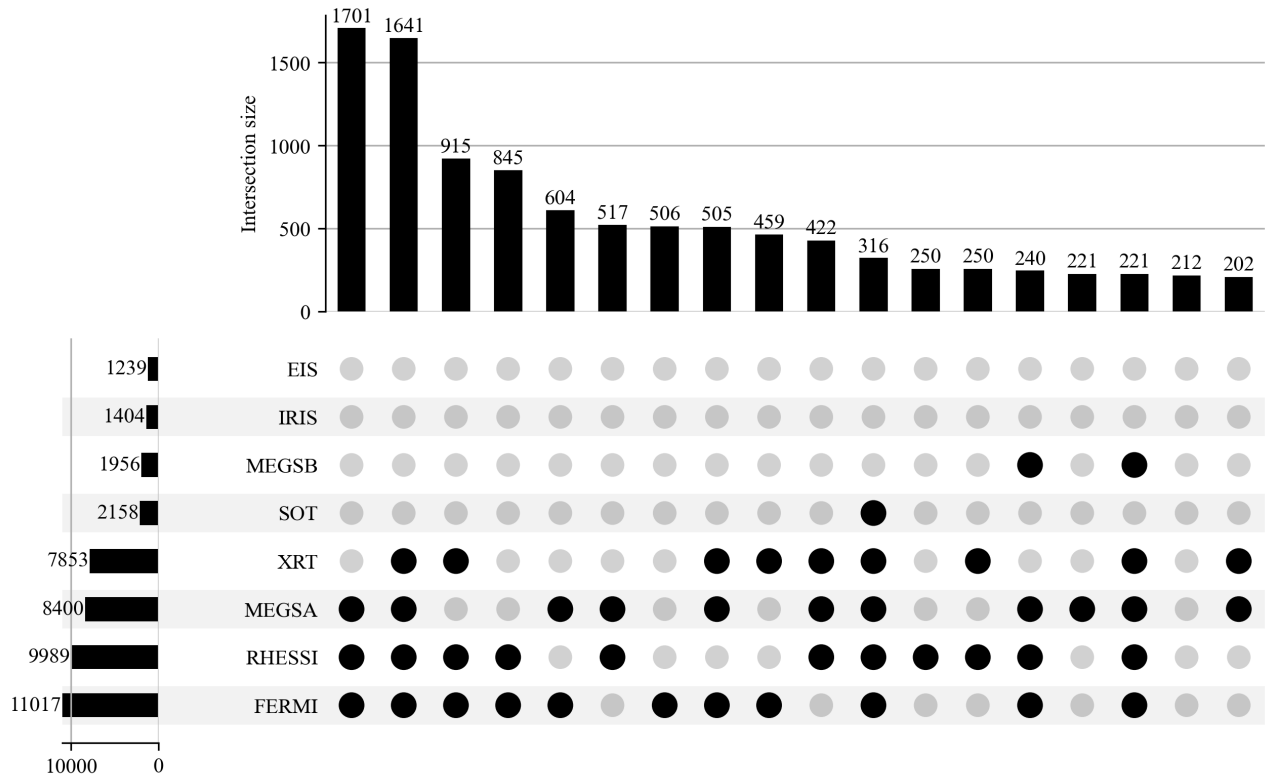


Figure 10: UpSet plot showing the intersection of sets of flares observed by each instrument. This plot is limited to subsets with more than 200 occurrences. From this plot, we can see that the most common collection of instruments to observe a solar flare is Fermi GBM, RHESSI and MEGS-A. It is also possible to see that Fermi GBM, RHESSI, MEGS-A and XRT all observed many more flares than the rest of the instruments. This is due to their FOV and duty cycles, as described in [Table 4](#).

was to maximise the number of events captured²⁷. In the similar analysis completed by [Milligan and Ireland \(2018\)](#), the same combination of instruments was found to be the most common in co-observing solar flares. As a result of the work described in [Section 2.2](#), it has been possible to catalogue a much larger number of flares into this subset with 930 flares catalogued in the previous study and 1,701 seen in [Figure 10](#).

An UpSet plot of the most well-observed flares with at least seven simultaneous observations is shown in [Figure 11](#). This provides an intuitive understanding of the instruments involved in making these multi-instrument observations. The combination of the seven instruments, excluding [IRIS](#), was responsible for observing 45 out of a total of 72 events observed by seven or more instruments. It should be noted from [Figure 5](#) that [IRIS](#) is the only sub-disk observing instrument which did not make observations throughout the entire time range in consideration which most likely resulted in its relatively low number of observed flares seen in [Figure 11](#).

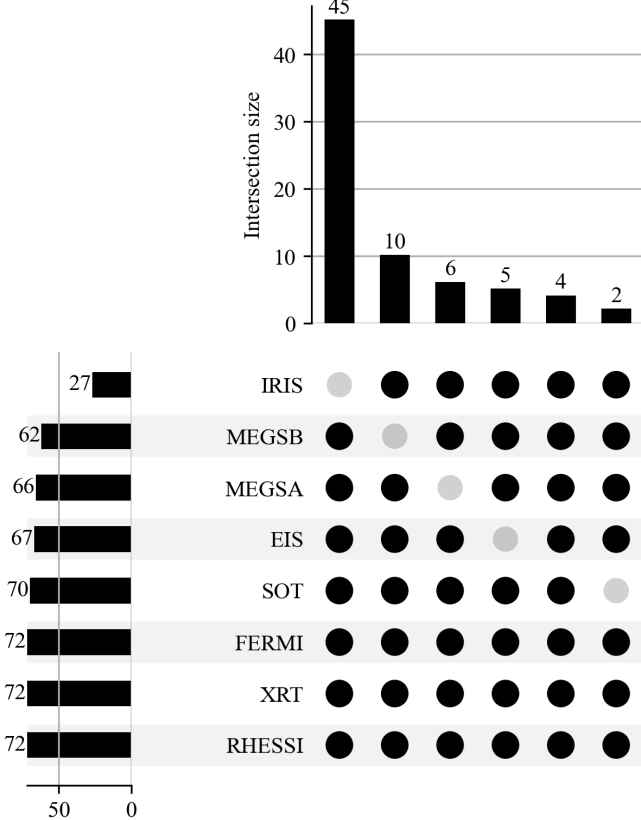


Figure 11: UpSet plot showing the intersection of sets of flares observed by each instrument for flares observed by seven or eight instruments simultaneously.

3.1.1 Expected Instrument Success Rates

With [Table 4](#), it is possible to investigate the performance of each of the instruments in observing solar flares. Estimated values for duty cycle and [FOV](#) have been taken from [Milligan and Ireland \(2018\)](#) and an expected success rate is calculated as the product of these two values. Two representations of the measured success rates of these instruments are presented for the time range in which all eight instruments were actively observing the Sun between 2013-Jul-07 and 2014-May-27. The difference between these two columns is their definition of an "observed" flare. The lenient definition is that a given flare is considered to be "observed" by an instrument if said instrument has made at least one measurement of the Sun between the flare's start and end times. With the lenient value of success rate, we can see that all instruments out-perform their expected success rates, indicative of intentional pointing of these instruments as opposed to random observations. [RHESSI](#) and [Fermi GBM](#) however, both out-perform their expected success rate significantly more than other instruments. The reason for this is most likely due to an inherent assumption that solar flares are instantaneous when calculating the lenient measured success rate. [Figure 12](#) was constructed with analysis of the flares included in this study and shows the distribution in flare duration for GOES Classes B, C, M and X. Solar flares are typically within the range of 15-25 minutes in duration with larger

²⁷As discussed previously, a lower [FOV](#) provides benefit in spatial resolution and a lower duty cycle may be necessary due to budget constraints / orbit.

Table 4: Estimates for the percentage of flares observed by a particular instrument as a product of their duty cycle and field of view. For instruments observing sub-full disk, the estimated success rate assumes a random pointing of the instrument. Based on the flare catalogue described in this report, the actual percentage of flares observed by each instrument during the period beginning 2010-Apr-30 and ending 2019-May-30 is calculated. *Lenient Measured Success Rate* imposes no restriction on the total fraction an instrument may have observed a given flare while strict measured success rate requires the instrument to have observed more than 50% of the flare to be considered "observed". Duty cycles and field-of-view estimations acquired from [Milligan and Ireland \(2018\)](#).

Instrument	Duty Cycle	%FOV	"Expected" Success Rate	Measured Success Rate (Lenient) ^a	Measured Success Rate (Strict) ^a
RHESSI	50%	100%	50%	77%	56%
SDO/EVE MEGS-A	100%	100%	100%	100%	100%
SDO/EVE MEGS-B	12.5%	100%	12.5%	11%	10%
Hinode/EIS	25%	2-25%	0.5-6%	7%	4%
Hinode/SOT	50%	1-17%	0.5-8%	17%	17%
Hinode/XRT	100%	25-100%	25-100%	53%	53%
IRIS	50%	0.5-3%	0.5-3%	11%	8%
FERMI GBM	50%	100%	50%	78%	56%

^aAs a percentage of the 1,737 flares occurring during all 8 of the instrument's lifetimes between 2013-Jul-17 and 2014-May-27.

flares lasting longer. As discussed previously, instruments in low Earth orbit are often prevented from making observations as a result of eclipse and **SAA** meaning blackouts will always occur at least once per orbit. With orbital periods of \approx 95 minutes, **RHESSI** and **Fermi GBM** both exit eclipse roughly 15 times every 24 hours and will encounter additional blackout-exiting events as a result of **SAA**. For each of these events, there is a chance that these instruments may observe the end of a solar flare, potentially making as little as one observation counting the flare as "observed" when using the lenient definition. This effectively increases the duty cycle by 15-25 minutes every time the instrument experiences a blackout-ending event, resulting in an inflated success rate (or an underestimated expected success rate). While **RHESSI** and **Fermi GBM** are the only instruments included in this study with a low Earth orbit, this theory may be backed up with the unique situation of **SDO/EVE MEGS-B**. Without sensor degradation, this instrument's expected success rate would have been 100% alongside **SDO/EVE MEGS-A**, however with the limited exposure of 3 hours per day, the instrument can be thought of as experiencing an artificial eclipse once every 24 hours. As a result, **SDO/EVE MEGS-B** also experiences blackout-ending events, however due to the significantly lower frequency compared to **RHESSI** and **Fermi GBM**, the lenient measured success rate will not be as inflated for **SDO/EVE MEGS-B**. This is reflected in **Table 4** as **SDO/EVE MEGS-B** has a lenient measured success rate of 11% and an expected success rate of 12.5%. In an attempt to compensate for

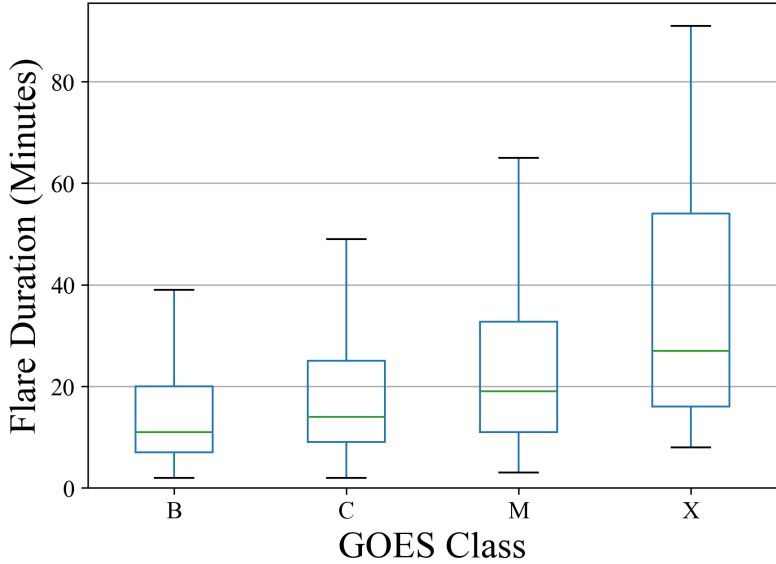


Figure 12: Box plots describing the distribution in flare length for flares of GOES class B, C, M and X. A general trend of increasing flare duration with respect to increasing peak soft X-ray flux is seen with an average flare duration for all flares of $\simeq 23$ min.

this effect, the strict definition of an "observed" flare is used; a given flare is considered to be "observed" by an instrument if that instrument has observed the Sun for more than 50% of the flare's duration. This results in a decrease in measured success rate for all instruments except [Hinode/SOT](#) and [Hinode/XRT](#)²⁸ however [RHESSI](#) and [Fermi GBM](#) see the largest reduction. This is further evidence that the duty cycle of these instruments is artificially increased as a result of eclipses and [SAA](#) which should be taken into account when interpreting the lenient measured success rate. All instruments are in line with or exceed the expected success rate, with [IRIS](#) significantly exceeding its expected success rate despite its low [FOV](#) and duty cycle. This reflects the high-priority of flare research and suggests a successful attempt in acquiring multi-instrument observations of solar flares.

3.1.2 Newly Discovered Exceedingly Well-Observed Flare

The four flares shown in [Table 5](#) were observed by all instruments considered in this study and present significant research potential. Three of these flares, SOL2014-02-01, SOL2014-02-03 and SOL2014-02-04 were included in the catalogue produced by [Milligan and Ireland \(2018\)](#), observed by the seven instruments included in that study and were found to also have been observed by [Fermi GBM](#). The C2.6 SOL2013-11-09 flare did not appear in the study completed by [Milligan and Ireland \(2018\)](#) due to a gap in data²⁹ within the [HEK](#) flare list, however with the incorporation of the [GOES](#) event list in [Section 2.2](#), it has been possible to identify this flare.

[Figure 13](#) displays light curves measured by [GOES](#), [RHESSI](#) and [Fermi GBM](#), representing

²⁸As a result of complexity introduced by rasterisation and data formatting, it was not possible to accurately determine the fraction of the total flare observed for [Hinode/XRT](#) and [Hinode/SOT](#). This would be a point of improvement for future study.

²⁹October – December 2012; July – November 2013; May 2014; February 2015; March and June 2016.

Table 5: Solar flares which have been simultaneously observed by RHESSI, SDO/EVE MEGS-A, SDO/EVE MEGS-B, Hinode/EIS, Hinode/SOT, Hinode/XRT, IRIS and Fermi GBM.

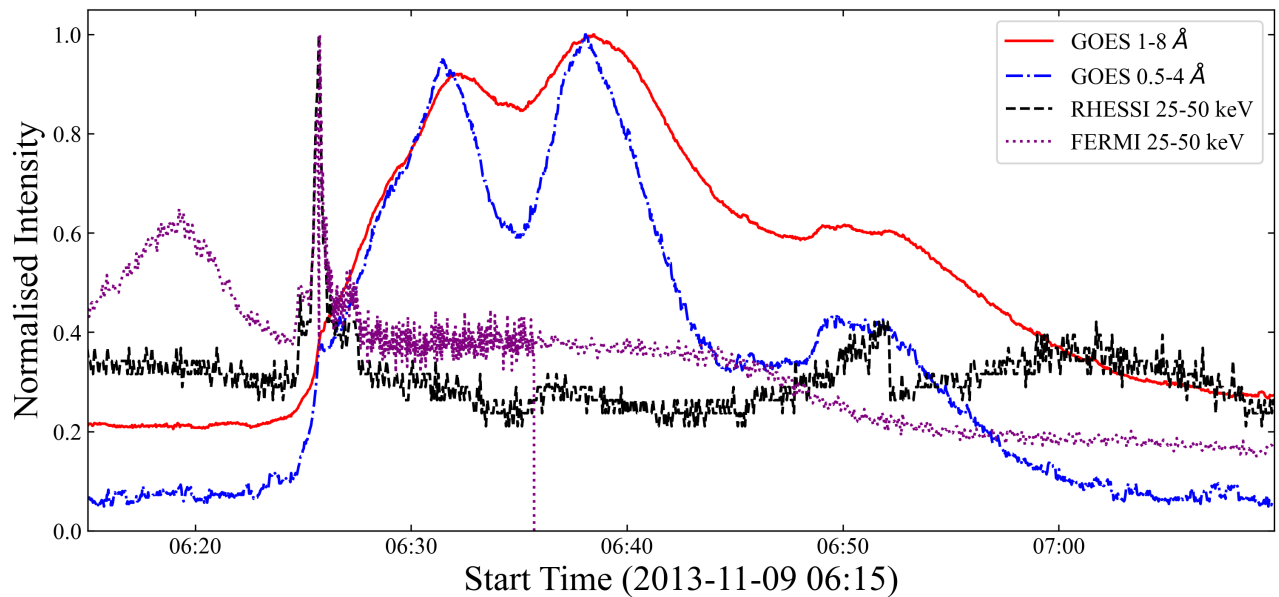
Flare Start	Flare Peak	Flare End	Class
2013-11-09 06:22	2013-11-09 06:38	2013-11-09 06:47	C2.6 ^a
2014-02-01 15:58	2014-02-01 16:05	2014-02-01 16:14	C2.3
2014-02-03 15:40	2014-02-03 15:43	2014-02-03 15:48	C4.6
2014-02-04 15:25	2014-02-04 16:02	2014-02-04 16:49	M1.5

^aNew well observed solar flare discovered during this study.

the **SXR** and **HXR** emission for this C-class flare. The Neupert effect can be seen in effect with the 25-50 keV, **HXR** peak during the impulsive phase before the **SXR** peak. This is indicative of non-thermal bremsstrahlung emission as a result of the accelerated non-thermal electrons described in the standard model. After the **HXR** peak, there is a more gradual increase in **SXR**, indicative of the thermal bremsstrahlung emission resulting from the hot plasma filling the magnetic field loops in the corona. **Figure 14** provides a more visual representation of the mechanisms involved in a solar flare with images taken by **SDO/AIA** at different wavelengths during the peak of the flare. In the 131 Å image, the hot plasma filling the loop is visible as bright lines in the SE - NW³⁰ direction. These lines are not visible in the 171 Å image, however as the plasma in the loop cools, it will begin to emit in longer wavelengths and appear in the 171 Å channel. The 304 Å channel images the Sun's chromosphere and it is here we can see two bright points which represent the flare's footpoints. Considering the light curves, location of the flare away from the limb and the structure as seen in the **SDO/AIA** images, this newly discovered well-observed C-class flare provides a good example of a well-observed standard model flare.

³⁰Note that for the Sun, North and South are in the expected locations but East is on the left side of the image and West is on the right.

Figure 13: Light curves as measured by the GOES X-Ray Sensor, RHESSI and Fermi GBM of the newly discovered well-observed flare, SOL2013-11-09.



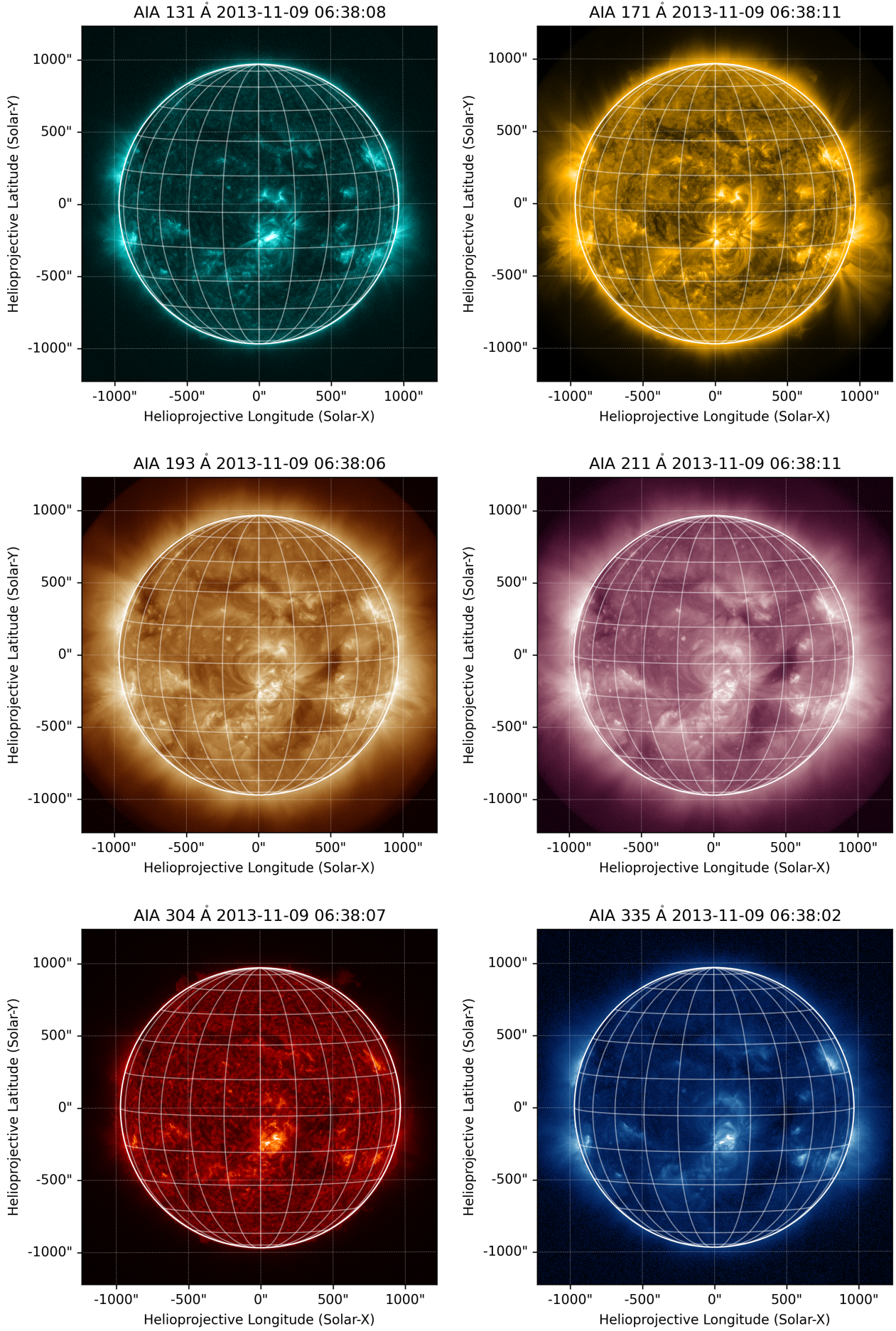


Figure 14: Images captured in different wavelengths by the Atmospheric Imaging Assembly onboard SDO of the newly discovered well-observed flare, SOL2013-11-09.

4 Summary

4.1 Further Study

Further study would increase the use cases for this catalogue through a number of improvements. An obvious step to improve the catalogue would be to increase the number of instruments included. Introducing ground-based radio observatories observing synchrotron emission from accelerated electrons would improve the effectiveness of the catalogue in searching for multi-wavelength observations of flares to be used in the research of acceleration methods. Additional space-based instruments such as the *Project for On-Board Autonomy-2* (PROBA-2: Santandrea et al. 2013) could be added and the expansion of the time range considered in this study would allow for the addition of newer instruments such as the *Advanced Space-based Solar Observatory* (ASO-S: Gan et al. 2019). Both of these instruments would be relatively simple to add as well as any instruments located on the Sun-Earth axis. With the assumption that all observations are made on this axis, determining whether an instrument is pointed at a flare is simplistic however, instruments orbiting the Sun as opposed to the Earth introduce complexity. For instruments such as *Solar Orbiter* (Müller et al., 2020) and *Solar TERrestrial RElations Observatory* (STEREO: Driesman et al. 2008), the relative positions of all instruments must be known in order to calculate observing angles relative to the Sun-Earth axis and by extension, determine whether the same flare has been observed by each instrument. Instruments off the Sun-Earth axis extend to those, much like *Fermi GBM*, which are not intended as solar instruments, but nevertheless provide valuable observations during solar flares. An example of the value of such multi-wavelength stereo observations of solar flares was presented by Lastufka et al. (2019), who investigated the M-class behind-the-limb solar flare SOL2013-05-01T02:32 using simultaneous observations made by RHESSI and the *Mars Odyssey* spacecraft (Saunders et al., 2004) orbiting Mars. These observations allowed for a better understanding of where non-thermal electrons exist during a flare as well as the ratio between non-thermal electrons in the high coronal source and non-thermal electrons in the footpoints.

Furthermore, the creation of an online dashboard to host the catalogue would greatly increase its usability. While the catalogue is suitable to be used in an online dashboard currently, there are some improvements which could be made in order to maximise the use cases. The addition of the fraction observed of the entire flare and the impulsive and gradual phases for Hinode/SOT and Hinode/XRT allow for more effective filtering. Additionally, the settings used during observations could also be recorded, with slit/slot size as well as rasterisation settings ("sit-and-stare", step size, etc) would provide powerful filters.

4.2 Conclusions

Using a combination of the [GOES](#) and [HEK](#) flare lists, it was possible to catalogue 14,458 flares between 2010-Apr-30 and 2019-May-30 and record corresponding successful observations made by a list of eight instruments. With the combined flare lists and an increased time range, it was possible to catalogue an extra 7,505 flares compared with previous studies while also including an eighth instrument; [Fermi GBM](#). Through an improved method of determining successful observations made by [RHESSI](#), it was possible to capture 18% more successful observations made by this instrument. In subsequent analysis of the catalogue, it was found that 98.5% of flares within the time range were observed by at least one instrument and on average, each flare was observed by three instruments. It was found that each of the instruments considered in this study met or exceeded their expected success rates with [IRIS](#) greatly exceeding its expected success rate of 0.5-3%, achieving an 11% success rate. The success rates calculated in this study were in agreement with previous studies, with variation accounted for as a difference in the method used to determine a successful observation. It was found that a total of 4 flares were observed by all 8 instruments; an M1.5 flare on the 2014-Feb-04, a C4.6 flare on the 2014-Feb-03, a C2.3 flare on the 2014-Feb-01 and a C2.6 flare on the 2013-Nov-09. The three 2014 flares were previously published by [Milligan and Ireland \(2018\)](#) and were found to also be observed by [Fermi GBM](#) however the 2013 flare was newly discovered and found to have complete coverage by all instruments with the exception of [IRIS](#) which missed 20% of the impulsive phase. Finally, it was found that the most common combination of instruments to observe a given flare within this time range was [SDO/EVE](#) [MEGS-A](#), [RHESSI](#) and [Fermi GBM](#) with the second most common combination being the same three instruments with the addition of [Hinode/XRT](#).

A Mount-Wilson Classification of Active Regions

Classification	Description
α	A unipolar sunspot group containing one or more sunspots. Opposite polarity remains present but is not concentrated enough to form sunspots.
β	A bipolar sunspot group with a simple neutral line between opposite polarities.
γ	A complex sunspot group with irregular / completely intermixed magnetic polarity.
δ	A sunspot group with oppositely polarised umbrae within a penumbra separated at most by 2° in heliographic distance.
$\gamma - \delta$	A γ sunspot group containing at least one δ sunspots.
$\beta - \gamma$	A bipolar sunspot group containing at least two sunspots or sunspot groups with more than one continuous neutral line.
$\beta - \delta$	A β sunspot group containing one or more δ sunspots.
$\beta - \gamma - \delta$	A $\beta - \gamma$ sunspot group containing one or more δ sunspots.

Table 6: The Mount-Wilson classification is used to describe active regions on the Sun. δ active regions are the most common region to observe solar flares. Adapted from He et al. (2021).

B Two Pointer Approach for Finding Interval Intersections

The problem of finding time ranges where a particular instrument is not in **SAA** and also not in eclipse can be simplified to finding the overlap between two lists of intervals. These intervals will be thought of as numerical intervals, i.e. $[(0, 4), (6, 8), (10, 11)]$, as opposed to time intervals for simplicity however it should be noted that ideas applied to the numeric interval approach also apply to the datetime approach.³¹ Following this simplification, the problem reduces to the following question:

Given that we have two sorted lists of intervals, A and B , return the intersection of the two interval lists.

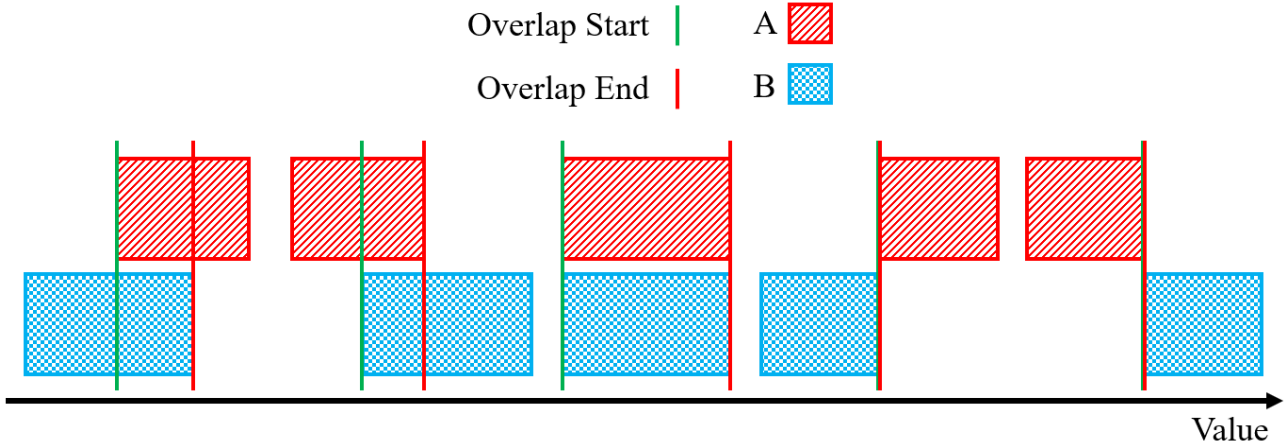


Figure 15: All possible overlaps between two lists of intervals, displayed on a number-line.

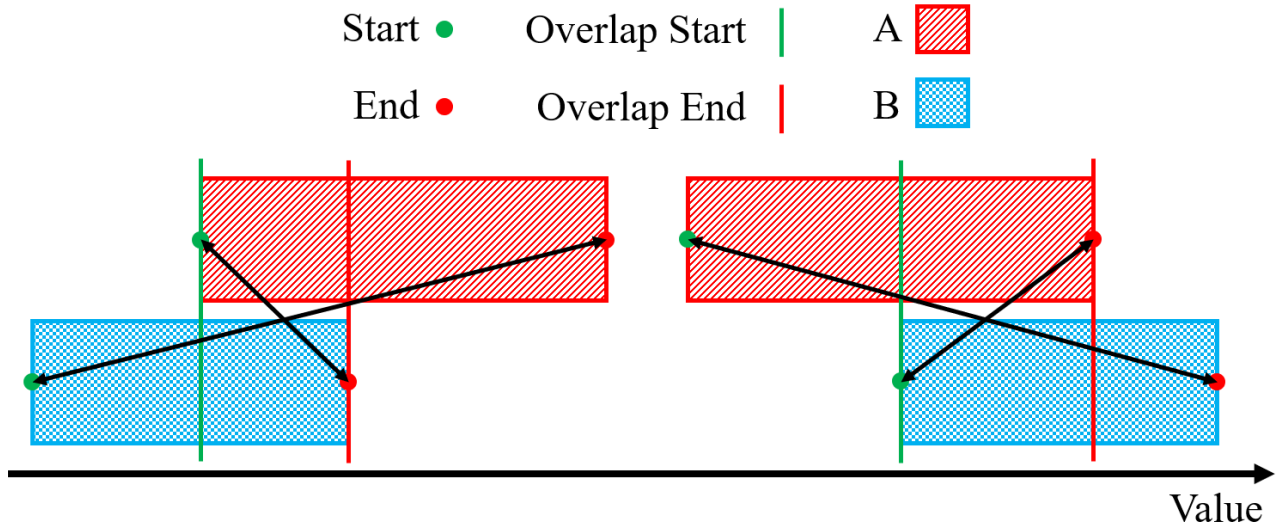


Figure 16: Two examples of overlapping intervals, defined as the range in which $A_{start} \leq B_{end}$ and $B_{start} \leq A_{end}$.

Each possible overlap is shown in **Figure 15** where lists A and B are shown on a number-line and the first two cases can be used to develop a definition of overlap. Where an overlap exists, the criss-cross pattern seen in **Figure 16** will satisfy the following conditions:

³¹For example, it is possible to represent a datetime as the number of seconds elapsed since a given date, commonly 1970-01-01. As a result, an algorithm to find overlaps in numeric time ranges will directly translate to finding overlaps in time ranges.

$$A_{start} \leq B_{end} \quad (3)$$

$$B_{start} \leq A_{end} \quad (4)$$

When both of these conditions are met, it is confirmed that an overlap exists between list A and B . To create a new list containing only the overlapping ranges, the following logic is used where C is the overlapping region:

$$C_{start} = \max(A_{start}, B_{start}) \quad (5)$$

$$C_{end} = \min(A_{end}, B_{end}) \quad (6)$$

Now that we have a method of determining if overlap exists and then the start and end points of said overlap, a two pointer approach may be used to step through each list, A and B . To do this, the pointers (one for each list) are incremented with respect to the end values, as shown visually in **Figure 17**. If the current A_{end} is less than or equal to the current B_{end} , the A range is exhausted and the next A interval should be considered, otherwise the B range is exhausted and a step should be taken through the B list.

$$\text{if } A_{end} \leq B_{end} \text{ then step forward in } A \quad (7)$$

$$\text{if } A_{end} > B_{end} \text{ then step forward in } B \quad (8)$$

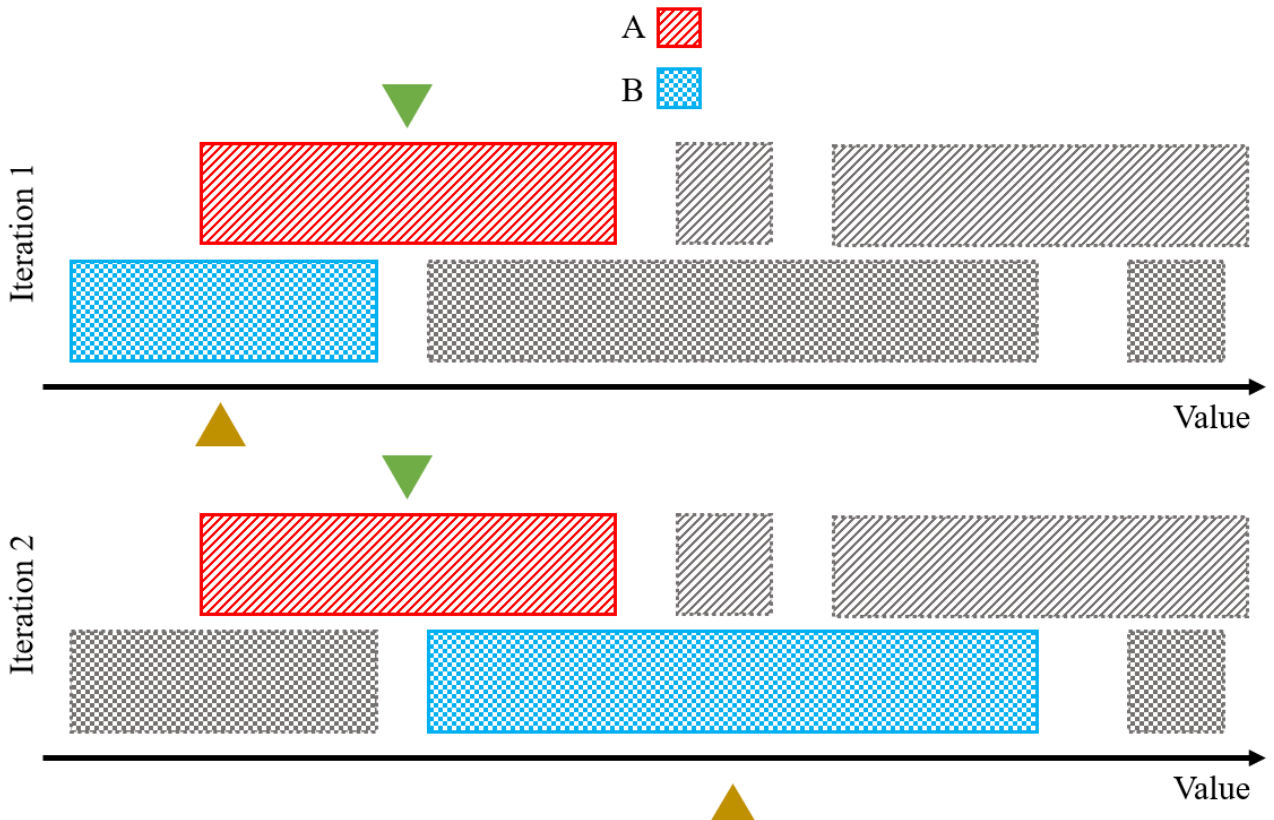


Figure 17: Visual representation of the step-wise motion of the two pointers through the two lists of intervals, A and B . Iteration continues until either list A or list B is exhausted.

Adapted from Leetcode solution by arkaung (2020) [Aung \(2020\)](#)

C RHESSI Flare Flag Inaccuracies

Below are light curves from **RHESSI**, **Fermi GBM** and **GOES** for M-class flares where **RHESSI** was not in eclipse or **SAA** but failed to flag the event as a flare. With the flares considered in this study, there were 1,519 cases where **RHESSI** had a clear view of a flare (not in eclipse or **SAA**) but failed to flag the event as a flare. This means that, if the **RHESSI** flare flags were used to determine a successful flare observation, 15% of all successful **RHESSI** observations would be excluded.

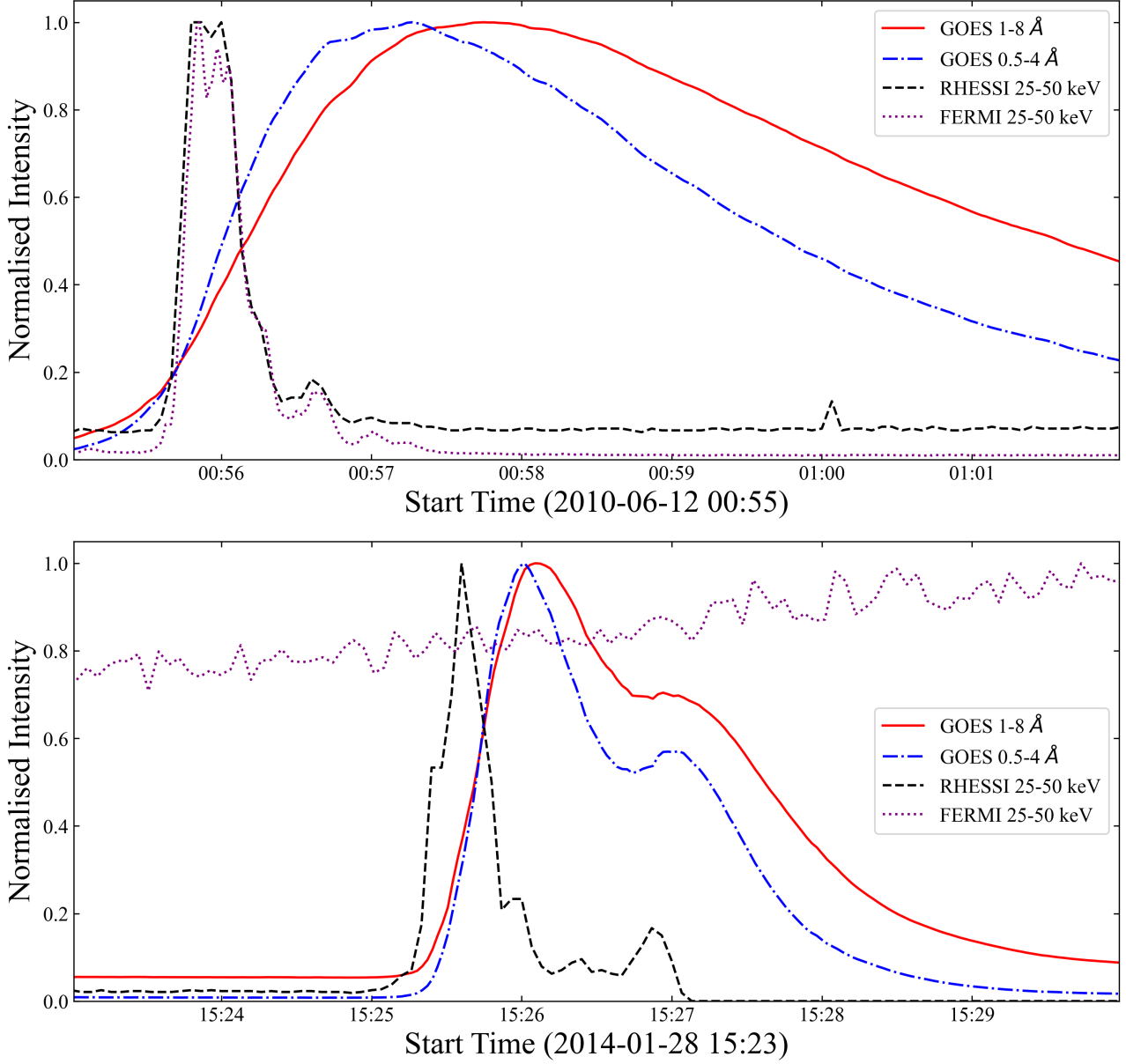


Figure 18: (*Top*) GOES, RHESSI and Fermi GBM light curves for M2.0 flare, SOL2010-06-12. Despite measuring a significant peak in hard X-Ray flux at 25-20 keV, this flare was not flagged as a flare by RHESSI. Fermi GBM observations made in the same energy band confirm the presence of a hard X-Ray peak. (*Bottom*) GOES, RHESSI and Fermi GBM light curves for M3.5 flare, SOL2014-01-28. Despite measuring a significant peak in hard X-Ray flux at 25-20 keV, this flare was not flagged as a flare by RHESSI. RHESSI data drops out at 15:27 as the instrument becomes occulted by the Earth. Fermi GBM was not observing the Sun during this flare, most likely as a result of eclipse due to the low variability in measurements.

References

- M. J. Aschwanden. *Physics of the Solar Corona. An Introduction with Problems and Solutions (2nd edition)*. 2005.
- A. M. Aung. [python] two pointer approach + thinking process diagrams - undefined, May 2020. URL <https://leetcode.com/problems/interval-list-intersections/solutions/647482/python-two-pointer-approach-thinking-process-diagrams/>.
- M. Battaglia, L. Kleint, S. Krucker, and D. Graham. How important are electron beams in driving chromospheric evaporation in the 2014 march 29 flare? *Astrophysical Journal*, 813, 11 2015. ISSN 15384357. doi:[10.1088/0004-637X/813/2/113](https://doi.org/10.1088/0004-637X/813/2/113).
- T. Bridgman. The best observed x-class flare, May 2023. URL <https://svs.gsfc.nasa.gov/11522>.
- D. A. Crotser, T. N. Woods, F. G. Eparvier, G. Ucker, R. A. Kohnert, G. D. Berthiaume, and D. M. Weitz. Sdo-eve multiple euv grating spectrograph (megs) optical design. volume 5563, page 182. SPIE, 10 2004. doi:[10.1117/12.560155](https://doi.org/10.1117/12.560155).
- J. L. Culhane, L. K. Harra, A. M. James, K. Al-Janabi, L. J. Bradley, R. A. Chaudry, K. Rees, J. A. Tandy, P. Thomas, M. C. Whillock, B. Winter, G. A. Doschek, C. M. Korendyke, C. M. Brown, S. Myers, J. Mariska, J. Seely, J. Lang, B. J. Kent, B. M. Shaughnessy, P. R. Young, G. M. Simnett, C. M. Castelli, S. Mahmoud, H. Mapson-Menard, B. J. Probyn, R. J. Thomas, J. Davila, K. Dere, D. Windt, J. Shea, R. Hagood, R. Moye, H. Hara, T. Watanabe, K. Matsuzaki, T. Kosugi, V. Hansteen, and Wikstol. The euv imaging spectrometer for hinode. *Solar Physics*, 243:19–61, 6 2007. ISSN 00380938. doi:[10.1007/s01007-007-0293-1](https://doi.org/10.1007/s01007-007-0293-1).
- A. Driesman, S. Hynes, and G. Cancro. The stereo observatory. *Space Science Reviews*, 136: 17–44, 4 2008. ISSN 00386308. doi:[10.1007/s11214-007-9286-z](https://doi.org/10.1007/s11214-007-9286-z).
- L. Farris and R. T. J. McAteer. Spatial and temporal analysis of 3 minute oscillations in the chromosphere associated with the x2.2 solar flare on 2011 february 15. *The Astrophysical Journal*, 903:19, 11 2020. ISSN 0004-637X. doi:[10.3847/1538-4357/abb701](https://doi.org/10.3847/1538-4357/abb701).
- L. Fletcher, B. R. Dennis, H. S. Hudson, S. Krucker, K. Phillips, A. Veronig, M. Battaglia, L. Bone, A. Caspi, Q. Chen, P. Gallagher, P. T. Grigis, H. Ji, W. Liu, R. O. Milligan, and M. Temmer. An observational overview of solar flares, 9 2011. ISSN 00386308.
- W. Q. Gan, C. Zhu, Y. Y. Deng, H. Li, Y. Su, H. Y. Zhang, B. Chen, Z. Zhang, J. Wu, L. Deng, Y. Huang, J. F. Yang, J. J. Cui, J. Chang, C. Wang, J. Wu, Z. S. Yin, W. Chen, C. Fang, Y. H. Yan, J. Lin, W. M. Xiong, B. Chen, H. C. Bao, C. X. Cao, Y. P. Bai, T. Wang, B. L. Chen, X. Y. Li, Y. Zhang, L. Feng, J. T. Su, Y. Li, W. Chen, Y. P. Li, Y. N. Su, H. Y. Wu, M. Gu, L. Huang, and X. J. Tang. Advanced space-based solar observatory (aso-s): An overview. *Research in Astronomy and Astrophysics*, 19, 2019. ISSN 16744527. doi:[10.1088/1674-4527/19/11/156](https://doi.org/10.1088/1674-4527/19/11/156).
- L. Golub, E. DeLuca, G. Austin, J. Bookbinder, D. Caldwell, P. Cheimets, J. Cirtain, M. Cosmo, P. Reid, A. Sette, M. Weber, T. Sakao, R. Kano, K. Shibasaki, H. Hara, S. Tsuneta, K. Ku-magai, T. Tamura, M. Shimojo, J. McCracken, J. Carpenter, H. Haight, R. Siler, E. Wright, J. Tucker, H. Rutledge, M. Barbera, G. Peres, and S. Varisco. The x-ray telescope (xrt) for the hinode mission. *Solar Physics*, 243:63–86, 6 2007. ISSN 00380938. doi:[10.1007/s11207-007-0182-1](https://doi.org/10.1007/s11207-007-0182-1).
- B. Harris. How are magnetic fields related to sunspots?, November 2007. URL https://soho.nascom.nasa.gov/explore/lessons/sunspots6_8.html.
- Y. He, Y. Yang, X. Bai, S. Feng, B. Liang, and W. Dai. Research on mount wilson magnetic classification based on deep learning. *Advances in Astronomy*, 2021, 2021. ISSN 16877977. doi:[10.1155/2021/5529383](https://doi.org/10.1155/2021/5529383).

- H. Hudson, E. Cliver, S. White, J. Machol, C. Peck, K. Tolbert, R. Viereck, and D. Zarro. *Solar physics*, 2023.
- P. G. Judge, T. D. Tarbell, and K. Wilhelm. A study of chromospheric oscillations using the soho and trace spacecraft. *The Astrophysical Journal*, 554(1):424, jun 2001. doi:[10.1086/321383](https://doi.org/10.1086/321383). URL <https://dx.doi.org/10.1086/321383>.
- L. Kleint, P. Heinzel, P. Judge, and S. Krucker. Continuum enhancements in the ultraviolet, the visible and the infrared during the x1 flare on 2014 march 29. *The Astrophysical Journal*, 816:88, 1 2016. ISSN 15384357. doi:[10.3847/0004-637x/816/2/88](https://doi.org/10.3847/0004-637x/816/2/88).
- E. Lastufka, S. Krucker, I. Zimovets, B. Nizamov, S. White, S. Masuda, D. Golovin, M. Litvak, I. Mitrofanov, and A. Sanin. Multiwavelength stereoscopic observation of the 2013 may 1 solar flare and cme. *The Astrophysical Journal*, 886:9, 11 2019. ISSN 15384357. doi:[10.3847/1538-4357/ab4a0a](https://doi.org/10.3847/1538-4357/ab4a0a).
- A. Lex, N. Gehlenborg, H. Strobelt, R. Vuillemot, and H. Pfister. Upset: Visualization of intersecting sets. *IEEE Transactions on Visualization and Computer Graphics*, 20(12):1983–1992, 2014. doi:[10.1109/TVCG.2014.2346248](https://doi.org/10.1109/TVCG.2014.2346248).
- R. P. Lin, B. R. Dennis, G. J. Hurford, D. M. Smith, A. Zehnder, P. R. Harvey, D. W. Curtis, D. Pankow, P. Turin, M. Bester, A. Csillaghy, M. Lewis, N. Madden, H. F. V. Beek, M. Appleby, T. Raudorf, J. McTiernan, R. Ramaty, E. Schmahl, R. Schwartz, S. Krucker, R. Abiad, T. Quinn, P. Berg, M. Hashii, R. Sterling, R. Jackson, R. Pratt, R. D. Campbell, D. Malone, D. Landis, C. P. Barrington-Leigh, S. Slassi-Sennou, C. Cork, D. Clark, D. Amato, L. Orwig, R. Boyle, I. S. Banks, K. Shirey, A. K. Tolbert, D. Zarro, F. Snow, K. Thomsen, R. Henneck, A. Mchedlishvili, P. Ming, M. Fivian, J. Jordan, R. Wanner, J. Crubb, J. Preble, M. Matranga, A. Benz, H. Hudson, R. C. Canfield, G. D. Holman, C. Crannell, T. Kosugi, A. G. Emslie, N. Vilmer, J. C. Brown, C. Johns-Krull, M. Aschwanden, T. Metcalf, A. Conway, and C. D. Rom. The reuven ramaty high-energy solar spectroscopic imager (rhessi), 2002.
- C. Meegan, G. Lichti, P. N. Bhat, E. Bissaldi, M. S. Briggs, V. Connaughton, R. Diehl, G. Fishman, J. Greiner, A. S. Hoover, A. J. V. D. Horst, A. V. Kienlin, R. M. Kippen, C. Kouveliotou, S. McBreen, W. S. Paciesas, R. Preece, H. Steinle, M. S. Wallace, R. B. Wilson, and C. Wilson-Hodge. The fermi gamma-ray burst monitor. *Astrophysical Journal*, 702:791–804, 2009. ISSN 15384357. doi:[10.1088/0004-637X/702/1/791](https://doi.org/10.1088/0004-637X/702/1/791).
- R. O. Milligan. Extreme ultra-violet spectroscopy of the lower solar atmosphere during solar flares (invited review). *Solar Physics*, 290:3399–3423, 12 2015. ISSN 1573093X. doi:[10.1007/s11207-015-0748-2](https://doi.org/10.1007/s11207-015-0748-2).
- R. O. Milligan and J. Ireland. On the performance of multi-instrument solar flare observations during solar cycle 24. *Solar Physics*, 293, 2 2018. ISSN 1573093X. doi:[10.1007/s11207-017-1233-x](https://doi.org/10.1007/s11207-017-1233-x).
- R. O. Milligan, G. S. Kerr, B. R. Dennis, H. S. Hudson, L. Fletcher, J. C. Allred, P. C. Chamberlin, J. Ireland, M. Mathioudakis, and F. P. Keenan. The radiated energy budget of chromospheric plasma in a major solar flare deduced from multi-wavelength observations. *The Astrophysical Journal*, 793, 10 2014. ISSN 15384357. doi:[10.1088/0004-637X/793/2/70](https://doi.org/10.1088/0004-637X/793/2/70).
- I. D. Moortel and P. Browning. Recent advances in coronal heating. *Philosophical Transactions of the Royal Society A: Mathematical, Physical and Engineering Sciences*, 373, 5 2015. ISSN 1364503X. doi:[10.1098/rsta.2014.0269](https://doi.org/10.1098/rsta.2014.0269).
- D. Müller, O. C. S. Cyr, I. Zouganelis, H. R. Gilbert, R. Marsden, T. Nieves-Chinchilla, E. Antonucci, F. Auchère, D. Berghmans, T. S. Horbury, R. A. Howard, S. Krucker, M. Maksimovic, C. J. Owen, P. Rochus, J. Rodriguez-Pacheco, M. Romoli, S. K. Solanki, R. Bruno, M. Carlsson, A. Fludra, L. Harra, D. M. Hassler, S. Livi, P. Louarn, H. Peter, U. Schühle, L. Teriaca, J. C. D. T. Iniesta, R. F. Wimmer-Schweingruber, E. Marsch, M. Velli, A. D. Groof, A. Walsh, and D. Williams. The solar orbiter mission: Science overview, 10 2020. ISSN 14320746.

- B. D. Pontieu, A. M. Title, J. R. Lemen, G. D. Kushner, D. J. Akin, B. Allard, T. Berger, P. Boerner, M. Cheung, C. Chou, J. F. Drake, D. W. Duncan, S. Freeland, G. F. Heyman, C. Hoffman, N. E. Hurlburt, R. W. Lindgren, D. Mathur, R. Rehse, D. Sabolish, R. Seguin, C. J. Schrijver, T. D. Tarbell, J. P. Wülser, C. J. Wolfson, C. Yanari, J. Mudge, N. Nguyen-Phuc, R. Timmons, R. van Bezooijen, I. Weingrod, R. Brookner, G. Butcher, B. Dougherty, J. Eder, V. Knagenhjelm, S. Larsen, D. Mansir, L. Phan, P. Boyle, P. N. Cheimets, E. E. DeLuca, L. Golub, R. Gates, E. Hertz, S. McKillop, S. Park, T. Perry, W. A. Podgorski, K. Reeves, S. Saar, P. Testa, H. Tian, M. Weber, C. Dunn, S. Eccles, S. A. Jaeggli, C. C. Kankelborg, K. Mashburn, N. Pust, L. Springer, R. Carvalho, L. Kleint, J. Marmie, E. Mazmanian, T. M. Pereira, S. Sawyer, J. Strong, S. P. Worden, M. Carlsson, V. H. Hansteen, J. Leenaarts, M. Wiesmann, J. Aloise, K. C. Chu, R. I. Bush, P. H. Scherrer, P. Brekke, J. Martinez-Sykora, B. W. Lites, S. W. McIntosh, H. Uitenbroek, T. J. Okamoto, M. A. Gummin, G. Auker, P. Jerram, P. Pool, and N. Waltham. The interface region imaging spectrograph (iris). *Solar Physics*, 289:2733–2779, 2014. ISSN 1573093X. doi:[10.1007/s11207-014-0485-y](https://doi.org/10.1007/s11207-014-0485-y).
- J. Qiu, D. E. Gary, and G. D. Fleishman. Evaluating mean magnetic field in flare loops. *Solar Physics*, 255:107–118, 3 2009. ISSN 00380938. doi:[10.1007/s11207-009-9316-y](https://doi.org/10.1007/s11207-009-9316-y).
- V. M. Sadykov, A. G. Kosovichev, V. Oria, and G. M. Nita. An interactive multi-instrument database of solar flares. *The Astrophysical Journal Supplement Series*, 231:6, 7 2017. ISSN 00670049. doi:[10.3847/1538-4365/aa79a9](https://doi.org/10.3847/1538-4365/aa79a9).
- S. Santandrea, K. Gantois, K. Strauch, F. Teston, E. Tilmans, C. Baijot, D. Gerrits, A. D. Groof, G. Schwemh, and J. Zender. Proba2: Mission and spacecraft overview. *Solar Physics*, 286:5–19, 8 2013. ISSN 1573093X. doi:[10.1007/s11207-013-0289-5](https://doi.org/10.1007/s11207-013-0289-5).
- R. S. Saunders, R. E. Arvidson, G. D. Badhwar, W. V. Boynton, P. R. Christensen, F. A. Cucinotta, W. C. Feldman, R. G. Gibbs, C. Kloss, M. R. Landano, R. A. Mase, G. W. McSmith, M. A. Meyer, I. G. Mitrofanov, G. D. Pace, J. J. Plaut, W. P. Sidney, D. A. Spencer, T. W. Thompson, and C. J. Zeitlin. 2001 mars odyssey mission summary, 2004.
- K. Shibata. Solar and stellar flares and their impact on planets. volume 11, pages 3–24. Cambridge University Press, 8 2015. doi:[10.1017/S1743921316006323](https://doi.org/10.1017/S1743921316006323).
- P. J. Simões, G. S. Kerr, L. Fletcher, H. S. Hudson, C. G. G. D. Castro, and M. Penn. Formation of the thermal infrared continuum in solar flares. *Astronomy and Astrophysics*, 605, 9 2017. ISSN 14320746. doi:[10.1051/0004-6361/201730856](https://doi.org/10.1051/0004-6361/201730856).
- I. M. Ternov. Synchrotron radiation. *Physics-Uspekhi*, 38(4):409, apr 1995. doi:[10.1070/PU1995v038n04ABEH000082](https://doi.org/10.1070/PU1995v038n04ABEH000082). URL <https://dx.doi.org/10.1070/PU1995v038n04ABEH000082>.
- S. Tsuneta, K. Ichimoto, Y. Katsukawa, S. Nagata, M. Otsubo, T. Shimizu, Y. Suematsu, M. Nakagiri, M. Noguchi, T. Tarbell, A. Title, R. Shine, W. Rosenberg, C. Hoffmann, B. Jurcevich, G. Kushner, M. Levay, B. Lites, D. Elmore, T. Matsushita, N. Kawaguchi, H. Saito, I. Mikami, L. D. Hill, and J. K. Owens. The solar optical telescope for the hinode mission: An overview. *Solar Physics*, 249:167–196, 6 2008. ISSN 00380938. doi:[10.1007/s11207-008-9174-z](https://doi.org/10.1007/s11207-008-9174-z).
- A. Veronig. The neupert effect. *Hvar Observatory Bulletin*, 27:47–58, 1 2003. URL <https://ui.adsabs.harvard.edu/abs/2003HvaOB..27...47V/abstract>.
- T. Wiegemann, J. K. Thalmann, and S. K. Solanki. The magnetic field in the solar atmosphere, 10 2014. ISSN 09354956.
- D. R. Williams, Nov 2022. URL <https://nssdc.gsfc.nasa.gov/planetary/factsheet/sunfact.html>.
- M. M. Woods, S. Inoue, L. K. Harra, S. A. Matthews, K. Kusano, and N. M. E. Kalmoni. The

triggering of the 2014 march 29 filament eruption. *The Astrophysical Journal*, 860:163, 6
2018. ISSN 15384357. doi:[10.3847/1538-4357/aac5e1](https://doi.org/10.3847/1538-4357/aac5e1).

T. N. Woods, F. G. Eparvier, R. Hock, A. R. Jones, D. Woodraska, D. Judge, L. Didkovsky,
J. Lean, J. Mariska, H. Warren, D. McMullin, P. Chamberlin, G. Berthiaume, S. Bailey,
T. Fuller-Rowell, J. Sojka, W. K. Tobiska, and R. Viereck. Extreme ultraviolet variability
experiment (eve) on the solar dynamics observatory (sdo): Overview of science objectives,
instrument design, data products, and model developments. *Solar Physics*, 275:115–143, 1
2012. ISSN 00380938. doi:[10.1007/s11207-009-9487-6](https://doi.org/10.1007/s11207-009-9487-6).